Available online at www.sciencedirect.com

Geochimica et Cosmochimica Acta 71 (2007) 5544–5564

Geochimica et Cosmochimica Acta

www.elsevier.com/locate/gca

Elemental and isotopic fractionation of Type B CAI-like liquids by evaporation

Frank M. Richter [a,b,c,*], Philip E. Janney [b,c,1], Ruslan A. Mendybaev [a,b], Andrew M. Davis [a,b,c,d], Meenakshi Wadhwa [a,b,c,1]

[a] *Department of the Geophysical Sciences, The University of Chicago, 5734 South Ellis Avenue, Chicago, IL 60637, USA*
[b] *Chicago Center for Cosmochemistry, 5734 South Ellis Avenue, Chicago, IL 60637, USA*
[c] *Department of Geology, The Field Museum, 1400 South Lakeshore Drive, Chicago, IL 60605, USA*
[d] *Enrico Fermi Institute, The University of Chicago, 5640 South Ellis Avenue, Chicago, IL 60637, USA*

Received 28 December 2006; accepted in revised form 12 September 2007; available online 21 September 2007

Abstract

Vacuum evaporation experiments with Type B CAI-like starting compositions were carried out at temperatures of 1600, 1700, 1800, and 1900 °C to determine the evaporation kinetics and evaporation coefficients of silicon and magnesium as a function of temperature as well as the kinetic isotope fractionation factor for magnesium. The vacuum evaporation kinetics of silicon and magnesium are well characterized by a relation of the form $J = J_o e^{-E/RT}$ with $J_o = 3.81 \times 10^6$ mol cm^{-2} s^{-1}, $E = 551 \pm 63$ kJ mol^{-1} for magnesium, $J_o = 4.17 \times 10^7$ mol cm^{-2} s^{-1}, $E = 576 \pm 36$ kJ mol^{-1} for silicon. These rates only apply to evaporation into vacuum whereas the actual Type B CAIs were almost certainly surrounded by a finite pressure of a hydrogen-dominated gas. A more general formulation for the evaporation kinetics of silicon and magnesium from a Type B CAI-like liquid that applies equally to vacuum and conditions of finite hydrogen pressure involves combining our determinations of the evaporation coefficients for these elements as a function of temperature ($\gamma = \gamma_0 e^{-E/RT}$ with $\gamma_0 = 25.3$, $E = 92 \pm 37$ kJ mol^{-1} for γ_{Si}; $\gamma_0 = 143$, $E = 121 \pm 53$ kJ mol^{-1} for γ_{Mg}) with a thermodynamic model for the saturation vapor pressures of Mg and SiO over the condensed phase. High-precision determinations of the magnesium isotopic composition of the evaporation residues from samples of different size and different evaporation temperature were made using a multicollector inductively coupled plasma mass spectrometer. The kinetic isotopic fractionation factors derived from this data set show that there is a distinct temperature effect, such that the isotopic fractionation for a given amount of magnesium evaporated is smaller at lower temperature. We did not find any significant change in the isotope fractionation factor related to sample size, which we interpret to mean that recondensation and finite chemical diffusion in the melt did not affect the isotopic fractionations. Extrapolating the magnesium kinetic isotope fractionations factors from the temperature range of our experiments to temperatures corresponding to partially molten Type B CAI compositions (1250–1400 °C) results in a value of $\alpha_{Mg} \approx 0.991$, which is significantly different from the commonly used value of $\alpha_{Mg} = 0.97977 = \sqrt{23.98504/24.98584}$.

1. INTRODUCTION

Recent laboratory studies have shown that molten silicates exposed to vacuum or to a low-pressure reducing gas become isotopically fractionated due to the lighter isotopes of the moderately volatile elements such as magnesium and silicon evaporating slightly faster than the heavier ones (Davis et al., 1990 using molten Mg_2SiO_4;

---

[*] Corresponding author. Fax: +1 773 702 9505.
E-mail address: richter@geosci.uchicago.edu (F.M. Richter).

[1] Present address: School of Earth and Space Exploration, Arizona State University, Box 871404, Tempe, AZ 85287, USA.

doi:10.1016/j.gca.2007.09.005

Wang et al., 2001 using a melt with solar proportions of major element oxides; Richter et al., 2002 with a Type B CAI-like composition melt). The composition used by Richter et al. (2002) was motivated by the observation that a certain component in primitive meteorites, the calcium-, aluminum-rich inclusions (CAIs), are often enriched in the heavy isotopes of silicon and magnesium (see Clayton et al., 1988), which is widely accepted as evidence that the isotopically fractionated inclusions were subjected to sufficiently high temperatures for a sufficiently long time in the solar nebula for them to partially melt and evaporate a fraction of their original silicon, magnesium, and associated oxygen. The CAIs that have been studied in the greatest detail are the large, coarse-grained CAIs from CV3 chondrites such as Allende. There are various reasons for this emphasis. These are the oldest materials generally accepted to have formed in the solar nebula (4.56711 ± 0.00016 Ga; Amelin et al., 2002, 2006), and their age is effectively that of the solar system. They are large enough that bulk magnesium and silicon isotopic analyses showing enrichment in the heavy isotopes have been available for more than twenty years. Coarse-grained CAIs can be divided into Type A, in which melilite and spinel are the dominant minerals, and Type B, which consist of melilite, a titanium-, aluminum-rich pyroxene commonly referred to as fassaite, spinel, and anorthite (Grossman, 1980). The Type B CAIs have petrologic features from which thermal histories have been inferred based on their igneous textures and mineral zoning (e.g., Stolper, 1982; MacPherson et al., 1984; Stolper and Paque, 1986). Grossman et al. (2000) used these various attributes to give the following plausible account for the origin and evolution of the Type B CAIs. (1) Precursors condensed as solids from an initially hot well-mixed gas of solar composition as temperatures fell to about 1100 °C. (2) The precursors were reheated by some unspecified mechanism to temperatures of about 1400 °C, which caused extensive melting and accounts for their igneous texture. (3) The partially molten stage lasted for a sufficient time that as much as 30% of the MgO component and 15% of the SiO_2 component evaporated, which accounts for the Type B CAIs being depleted in these components relative to compositions calculated to condense from a gas of solar composition and for the remaining silicon and magnesium to have become isotopically heavy. Assessing the validity of this or any other proposed scenarios for the origin and evolution of primitive materials in the early solar system requires quantifying the elemental and isotopic fractionations associated with evaporation and comparing these to observed fractionations. Such quantification requires reliable experimental data of various sorts, most importantly, thermodynamic data for calculating the equilibrium relationships between relevant phases and kinetic data for the elemental and isotopic fluxes associated with evaporation. The goal of the experimental study reported here is to extend and improve the kinetic database relevant to evaporation of Type B CAI-like liquids.

Quantitative calculations of the condensation sequence of a cooling gas of a specified pressure and composition are no better than the thermodynamic data used to calculate solid–liquid–gas equilibria. And while condensation calculations for the early solar nebula have a long history (e.g., Urey, 1952; Larimer and Anders, 1967; Grossman, 1972), significant uncertainties remain, reflecting different choices for the thermodynamic properties of the condensed phases (see discussions in Petaev and Wood, 2005 and Ebel, 2006). The fact of the matter is that comprehensive thermodynamic data do not yet exist for some of the most important compositions relevant to cosmochemistry. For example, the most complete model for calculating the thermodynamic properties of silicate liquids and partial melts is the MELTS computer code (Ghiorso and Sack, 1995) but the range of compositions it covers does not include chondritic or CAI-like compositions. The model of Berman (1983) for CaO–MgO–Al_2O_3–SiO_2 (CMAS) melts can be used for CAI-like compositions, but there is not yet a thermodynamic model for calculating solution properties in the full range from CAI-like melts to chondritic compositions. Serious uncertainties also arise with regards the thermodynamic properties of key minerals, especially when they involve solid solutions. The effect of such uncertainties can be seen when comparing the calculated and experimentally determined crystallization temperature of the major Type B CAI mineral melilite (a solid solution between gehlenite, $Ca_2Al_2SiO_7$, and åkermanite, $Ca_2MgSi_2O_7$). Grossman et al. (2002) calculated crystallization temperatures of melilite from a Type B CAI-like melt that were as much as 150 °C higher than that found in laboratory crystallization experiments with the same composition (Mendybaev et al., 2006). The crystallization temperatures for melilite in Type B CAI-like melts are extremely important in that these temperatures are the most direct constraint we have on the peak temperatures responsible for partially melting the Type B CAI precursors. Uncertainties regarding the composition of condensates from a solar composition gas and melilite crystallization temperatures are of concern for the present study in terms of our choosing relevant starting compositions and run temperatures for our evaporation experiments and how the results will be used to interpret the conditions experienced by the Type B CAIs and the nature of their precursors. We assume that the peak temperature and crystallization interval of the Type B CAI precursors is 1400–1250 °C based on the experimental data of Mendybaev et al. (2006). However, in order to avoid the difficulty of interpreting fractionation data when the condensed phase is not fully molten, we ran our evaporation experiments at somewhat higher temperatures than those likely to have been experienced by the Type B CAIs. The evaporation experiments reported here cover a sufficient temperature range of 1900–1600 °C to allow extrapolation of the results to the lower temperature range likely to have been experienced by the natural CAIs. The usual assumption, based on textural evidence (i.e., large euhedral melilite crystals), is that the Type B CAIs were reheated to only slightly above the melting temperature of melilite (~1400 °C) and remained partially molten down to temperatures of about 1250 °C (Stolper and Paque, 1986; Mendybaev et al., 2006).

2. THEORETICAL FRAMEWORK

The specific needs for experimental data in connection with the causes and consequences of evaporation are most easily seen with reference to the generally accepted theoretical representation of the evaporation/condensation process. The net evaporation flux of an element or isotope i from a condensed phase to a surrounding gas is given by (see Hirth and Pound, 1963)

$$J_i = \frac{n_i \gamma_i (P_{i,\mathrm{sat}} - P_i)}{\sqrt{2\pi m_i RT}}, \tag{1}$$

where the simplifying assumption (reasonable for our purposes) that the gas is dominated by a single species containing i has been made. J_i is the net flux of i in moles per unit area per unit time, n_i is the number of atoms of i in the gas species molecule, γ_i is the evaporation coefficient, $P_{i,\mathrm{sat}}$ is the saturation vapor pressure of i, P_i is the pressure of i at the evaporating surface, m_i is the molar mass of gas species containing i, R is the gas constant, and T is absolute temperature. This representation derives from the kinetic theory of ideal gases where $P_i/\sqrt{2\pi m_i RT}$ is the rate of collision with the surface of the species containing i. If only a fraction γ_i of the molecules impinging on the surface stick (i.e., condense), then the condensation flux of i will be reduced by this factor γ_i. At equilibrium, $P_i = P_{i,\mathrm{sat}}$ and there is no net flux of i from the condensed phase, thus an evaporation flux proportional to $P_{i,\mathrm{sat}}$ must balance the condensation flux. Eq. (1) follows from the assumption that the evaporation flux remains proportional to $P_{i,\mathrm{sat}}$ for all values of P_i including zero (i.e., evaporation into vacuum).

The experiments discussed in later sections involve conditions such that $P_i \ll P_{i,\mathrm{sat}}$ and the dominant gas species for silicon and magnesium are Mg and SiO, thus $n_i = 1$. Eq. (1) then becomes

$$J_i = \frac{\gamma_i P_{i,\mathrm{sat}}}{\sqrt{2\pi m_i RT}}. \tag{2}$$

The reason experimental data are essential for quantifying the evaporation kinetics of volatile elements from condensed phases is that the evaporation coefficients γ_i are often significantly different from unity, but there is no theoretical way of calculating them for the systems of interest here. In a later section, we present new experimental results for the evaporation rate of silicon and magnesium as a function of temperature and show that the associated evaporation coefficients are temperature dependent and very much smaller than one.

Eq. (2) can be used to define the relative volatility of elements during evaporation, which for silicon and magnesium we can write as

$$\frac{J_{\mathrm{Si}}}{J_{\mathrm{Mg}}} = \frac{\gamma_{\mathrm{Si}} P_{\mathrm{SiO,sat}}}{\gamma_{\mathrm{Mg}} P_{\mathrm{Mg,sat}}} \sqrt{\frac{m_{\mathrm{Mg}}}{m_{\mathrm{SiO}}}}. \tag{3}$$

The relevant masses are those of the dominant gas phase species containing magnesium and silicon in equilibrium with a CMAS melt (i.e., Mg and SiO). Note that the relative "kinetic" volatility of two elements during evaporation given by Eq. (3) could be quite different from the more usual definition of volatility given by the ratio of saturation vapor pressures alone. It follows from Eq. (3) that given a thermodynamic model for the CMAS liquid with which to calculate the saturation vapor pressures and laboratory data on the trajectory in composition space of the evaporation residues, the ratio of the evaporation coefficients can be determined. In a later section we will show that this approach can be used to determine the ratio of the magnesium and silicon evaporation coefficients as a function of temperature far more precisely than can be done by taking the ratio of evaporation coefficients measured separately.

Eq. (2) can also be used to represent the kinetic fractionation of isotopes by evaporation under the conditions where Eq. (2) is applicable (i.e., $n_i = 1$ and $P_i \ll P_{i,\mathrm{sat}}$). The ratio of the flux of two isotopes i and k of a given element is given by

$$\frac{J_i}{J_k} = \frac{\gamma_i P_{i,\mathrm{sat}}}{\gamma_k P_{k,\mathrm{sat}}} \sqrt{\frac{m_k}{m_i}}. \tag{4}$$

The usual practice is to rephrase the ratio of the isotopic fluxes in terms of a fractionation factor α_{ik}, defined as the ratio of the fluxes of individual isotopes, J_i/J_k, divided by the atom ratio of the isotopes in the condensed phase, N_i/N_k. The equilibrium isotopic fractionation factor $\alpha_{ik}^{\mathrm{Eq}}$ is defined by

$$\alpha_{ik}^{\mathrm{Eq}} \equiv \left(\frac{P_{i,\mathrm{sat}}}{P_{k,\mathrm{sat}}}\right) \Big/ \left(\frac{N_i}{N_k}\right), \tag{5}$$

and corresponds to the ratio of the isotopic composition of gas in equilibrium with the condensed phase to the isotopic composition of the condensed phase. Eqs. (4) and (5) are then used to write the fractionation factor α_{ik} as

$$\alpha_{ik} = \left(\frac{J_i}{J_k}\right) \Big/ \left(\frac{N_i}{N_k}\right) = \alpha_{ik}^{\mathrm{Eq}} \left(\frac{\gamma_i}{\gamma_k}\right) \sqrt{\frac{m_k}{m_i}} = \alpha_{ik}^{\mathrm{Eq}} \alpha_{ik}^{\mathrm{Kin}}. \tag{6}$$

Eq. (6) shows that the isotopic fractionation factor for evaporation is the product of an equilibrium isotope fractionation factor $\alpha_{ik}^{\mathrm{Eq}}$ defined by Eq. (5) times a kinetic isotope fractionation factor $\alpha_{ik}^{\mathrm{Kin}} \equiv (\gamma_i/\gamma_k)\sqrt{m_k/m_i}$.

The isotope fractionation factor α_{ik} is the key quantity relating the isotopic fractionations of an evaporation residue to the amount of parent element evaporated. The usual formulation of this relationship is the Rayleigh fractionation equation,

$$\frac{R_{ik}}{R_{ik,0}} = f_k^{\alpha_{ik}-1}, \tag{7}$$

where $R_{ik,0}$ is the isotopic ratio N_i/N_k in the condensed phase prior to evaporation and R_{ik} is the isotopic ratio in the evaporation residue when a fraction f_k of isotope k remains (see Richter, 2004, for a derivation and discussion of the conditions when Eq. (7) can be used for evaporation residues). The importance of Eq. (7) in the context of CAI studies is that the isotopic composition R_{ik} of an inclusion, together with the experimentally determined value of the isotope fractionation factor α_{ik} and the assumption that the isotopic composition of the precursor was isotopically unfractionated relative to bulk solar system material, allows one to calculate the fraction f_k of isotope k remaining. Given the smallness of the isotopic fractionations of CAIs, the fraction of the parent element of k remaining is, for all practical purposes, the same as f_k and, from this, one can determine the original amount of the element in the precursor. Once the composition of the precursor has been determined, one can address the question of whether the precursor corresponds to a plausible condensate from a solar composition gas (see Grossman et al., 2000, for a discussion of this approach). The fraction of volatile elements evaporated can also be used, together with laboratory-measured evaporation kinetics as a function of temperature, to constrain thermal histories that could have produced the observed loss of the volatile elements by evaporation (see Richter et al., 2002, 2006, for examples of this approach).

Two common assumptions made in connection with Eq. (6) are that the equilibrium isotopic fractionations are negligible at the temperatures required to partially melt CAIs (i.e., $\alpha_{ik}^{\mathrm{Eq}} = 1$ for $T \sim 1400\ °\mathrm{C}$) and that the evaporation coefficients of isotopes of a given element are the same (i.e., $\gamma_i/\gamma_k = 1$). The attractiveness of these assumptions is that they make the isotopic fractionation factor for evaporation an easily calculated quantity based on nothing more than the relative mass of the isotopically distinct gas species. The question we need to address is what is the evidence for these two simplifying assumptions? In the case of silicate liquids, direct experimental evidence for the first of these assumptions is, as far as we are aware, limited to two experiments reported by Richter et al. (2002) showing that the magnesium isotopes in residues evaporated at 1400 °C in a furnace with one bar of slowly flowing hydrogen were not measurably fractionated. The flow rate of the hydrogen gas was sufficiently slow for the evaporated species to be effectively in equilibrium with the molten sample. The slow but continuous removal of the equilibrium gas will result in a residue with elements fractionated in proportion to their relative saturation pressures and isotopes in proportion to any equilibrium isotopic fractionation between the gas and the melt. We found that one residue lost 23.8% of its original magnesium and had a magnesium isotopic composition of $-0.40 \pm 0.48‰$ per amu relative to the starting composition. A second residue had lost 60.1% of the magnesium and an isotopic composition of $0.26 \pm 0.57‰$ per amu relative to the starting composition. These data result in an estimate of $\alpha_{ik}^{\mathrm{Eq}} = 0.99989 \pm 0.00060(2\sigma)$, which at least for magnesium, justifies the assumption that the equilibrium isotope fractionation between a CMAS liquid and gas at 1400 °C is negligible compared to the expected kinetic isotope fractionation.

Evidence that $\gamma_i/\gamma_k = 1$ for evaporation of molten oxides or silicates, and therefore that $\alpha_{ik}^{\mathrm{Kin}} = \sqrt{m_k/m_i}$, has been found experimentally only for iron evaporating into vacuum from molten FeO (Wang et al., 1994; Dauphas et al., 2004) and for one set of experiments involving potassium evaporating from a molten chondrule-like composition (Yu et al., 2003). However, Dauphas et al. (2004) also showed that the isotopic fractionation of iron evaporating from molten silicate liquids is significantly less than that calculated using a fractionation factor equal to the inverse square root of the mass of the iron isotopes. The implication is that even for the same element the ratio γ_i/γ_k for isotopes can equal or differ from one depending on the composition of the condensed phase. Davis et al. (1990) and Wang et al. (2001) reported vacuum evaporation data showing that the kinetic isotope fractionation of magnesium, silicon and oxygen evaporating from silicate liquids (molten Mg_2SiO_4 in Davis et al. (1990), a molten mixture of major oxides in solar proportions in Wang et al., 2001) was significantly less than that calculated using $\alpha_{ik}^{\mathrm{Kin}} = \sqrt{m_k/m_i}$. Richter et al. (2002) carried out a series of CMAS evaporation experiments in both vacuum ($P < 10^{-6}$ Torr) and in hydrogen ($P_{\mathrm{H2}} \approx 2 \times 10^{-4}$ bars) and found magnesium isotopic fractionations that were again significantly less than those calculated assuming a kinetic isotope fractionation factor equal to the inverse square root of the mass of the magnesium isotopes. A recurring concern has been that the reported smaller than expected kinetic isotope fractionations may have been experimental artifacts due to recondensation or that diffusion was not sufficiently fast to maintain the homogeneity of the condensed phase. The latter concern is easily dismissed for the experiments reported here, in that the quenched evaporation residues were in every case found to be chemically homogeneous. This is as expected given the size samples that were used, the duration of the experiments, and the chemical diffusivities in silicate melts at the temperature of our experiments. The issue of recondensation effects is a bit more complicated. In the Appendix A, we discuss the effect of recondensation on the isotopic fractionation of residues in the case of evaporation into a surrounding gas and in a vacuum furnace of finite gas conductance. Interestingly, the effect on isotopic fractionation of recondensation due to a surrounding gas and in a system of finite gas conductance are opposite. In the case of evaporation into a surrounding gas the isotopic fractionation for a given amount of parent element evaporated is reduced, whereas in a system of finite gas conductance the isotopic fractionation will, if anything, be increased. It follows that when one finds the isotopic fractionation of laboratory evaporation residues to be less than that corresponding to the fluxes being inversely proportional to mass, the reason cannot be recondensation. We also tested the degree to which recondensation might have affected the isotopic fractionation of our evaporation residues using samples of significantly different surface area. If recondensation effects had been important, the larger samples would have been the most affected.

The main objective of our undertaking the new set of vacuum evaporation experiments reported here is to provide high-precision data with which to resolve the issue of the appropriate kinetic isotopic fractionation factor for magnesium that should be used to relate the measured isotopic fractionation of Type B CAIs to the amount of magnesium volatilized. As noted earlier, establishing the relationship between isotopic and elemental fractionations by evaporation is the essential tool for reconstructing the composition and thermal history of the precursors of isotopically fractionated CAIs. The present study has a number of advantages over that reported in Richter et al. (2002), including: (1) significantly greater precision (~10×) in measuring the magnesium isotopic composition of the evaporation residues by multicollector inductively coupled plasma mass spectrometer (MC-ICPMS) compared to the earlier measurements done using a single-collector ion microprobe; (2) a large number of samples of different surface areas with which to assess recondensation effects; and (3) a range of evaporation temperatures that show that the kinetic isotope fractionation factor is significantly affected by the temperature at which evaporation takes place. An important additional point is that the isotopic composition of the evaporation residues that we report here was measured on magnesium that had been separated from the other major cations by ion exchange to remove biases due to matrix effects. And while the main focus of the work is on the isotopic fractionation of the evaporation residues, the experiments also provide information on the elemental fractionation and evaporation kinetics of silicon and magnesium over a larger temperature range than previously reported in Richter et al. (2002).

3. EXPERIMENTAL AND ANALYTICAL METHODS

3.1. Starting materials and experimental procedure

The starting materials for the evaporation experiments were prepared in 1-g batches by mixing appropriate amounts of high-purity (>99.99%) SiO_2, Al_2O_3, MgO, and $CaCO_3$, which, when decarbonated, produced a Type B CAI-like composition. The mixture was ground under ethanol in an agate mortar for at least 1 h, dried in air at room temperature, and then placed in a platinum crucible to be slowly heated in a muffle furnace to 1000 °C, and held at this temperature for 5–10 h in order to drive off the CO_2 released as $CaCO_3$ decomposed. The platinum crucible was then transferred to a one-atmosphere Deltech vertical tube furnace where the mixture was melted under oxidizing conditions (in air) at 1500 °C for about 24 h, after which it was rapidly quenched to produce a clear glass. The quenched glass was ground to a fine powder and then used to make the experimental samples by loading 5–200 mg aliquots mixed with polyvinyl alcohol onto iridium wire (0.25 mm diameter) loops with inside diameters ranging from 1 mm to 6 mm. The samples were then heated in a Deltech vertical-tube furnace for one hour at 1000 °C in air to drive off the polyvinyl alcohol and sinter the powder such that the samples could be weighed. The final step in preparing the experimental samples was to partially melt them again by putting them back into the Deltech furnace at 1400 °C for several hours. The iridium wire loops with the partially molten samples were removed from the furnace, weighed again, and the dimensions of the loops and the thickness of samples at the center of the loop measured using a micrometer. These steps do not result in any measurable mass loss by evaporation of either the iridium wire or the sample. The major-element composition of the starting materials is given in Table 1.

The evaporation experiments were carried out at the University of Chicago using a high-temperature vacuum furnace designed and constructed by Hashimoto (1990). At run conditions, the pressure outside the heating elements and heat shields surrounding the sample was always less than 10^{-6} Torr. The temperature at the sample was measured by two Type G (W vs. $W_{0.74}Re_{0.26}$) thermocouples, each within 1 cm of the sample. Calibration experiments over a temperature range of 1600–2000 °C, in which the thermocouple-determined temperatures were compared to those made with a PYRO Micro-Optical pyrometer, showed agreement among the various temperature measurements to within ±5 °C. The temperature history of the experiments involved preheating the furnace to 900 °C in about an hour in manual mode, followed by heating in automatic mode at a rate 20.0 °C min^{-1} to 1400 °C. This temperature was held for 20 min to ensure complete degassing of the sample, followed by raising the temperature at 20.0 °C min^{-1} to the final run temperature of 1600, 1700, 1800, or 1900 °C. A Eurotherm controller was used to maintain the run temperature to within a few degrees, and the run was ended by cutting the power to the heating elements so that the samples cooled to room temperature in a few minutes. The cooling was sufficiently fast for the evaporation residues to be quenched to glass. Control experiments in which samples were quenched after heating for 20 min at 1400 °C showed that no measurable weight loss or magnesium isotopic fractionation occurred during the degassing step.

In order to measure evaporation fluxes, the surface area of each sample must be known. The starting and final weight and maximum thickness perpendicular to the plane of the iridium loop was measured for all samples. An equivalent thickness for an ellipsoid of a given diameter and weight corresponding to that of each of our samples was calculated using the density–composition–temperature relations of Lange and Carmichael (1987) and the thermal expansion of iridium. The calculated thicknesses were $21 \pm 6\%$ larger than measured on the 1 mm samples, $2 \pm 4\%$ larger than those measured on the 2.5 mm samples, and $13 \pm 3\%$ smaller than measured on the 6 mm samples. We believe the calculated sample thicknesses are more realistic than the directly measured values because they take into account the volume at the high temperatures of the experiments and also avoid potential problems with trapped bubbles that would exaggerate the volume of the starting materials. We observed that about half of the 0.25 mm iridium wire was typically wetted by melt, and to take this into account we used an effective sample diameter 0.25 mm larger than the inner diameter of the iridium loops. The effective diameters of the samples were thus 1.25 mm, 2.75 mm, 3.55 mm, and 6.25 mm. We estimated an uncertainty due to whether or not the wetted wire represented an additional evaporating surface by comparing the surface area calculated using these effective loop diameters to those calculated using this diameter augmented or reduced by 0.25 mm (i.e., assuming the entire loop was either entirely wetted or not wetted at all). The difference in calculated surface area for a diameter $D = 1.25 \pm 0.25$ was +16% and −13% compared to $D = 1.25$ mm, for $D = 2.75 \pm 0.25$ mm the difference was +8% and −6% compared to $D = 2.75$ mm, while for $D = 6.25 \pm 0.25$ mm the difference was +5% and −4% compared to $D = 6.25$ mm. The surface areas we used to calculate evaporation fluxes are those derived using the effective diameter and the calculated sample thicknesses rather than the measured thick-

Table 1
Experimental conditions of vacuum evaporation experiments, elemental and isotopic composition of the evaporation residues, and calculated evaporation rates of magnesium and silicon from a Type B CAI-like melt

Sample	Diam (mm)	Run time (min)	MgO (wt%)	SiO_2 (wt%)	Al_2O_3 (wt%)	CaO (wt%)	Init[a] area (mm^2)	Final[a] area (mm^2)	Init wt mg	% Mass loss	% Mg loss	J_{Mg}[a] (mol cm^{-2} s^{-1})	J_{Si}[a] (mol cm^{-2} s^{-1})	δ^{25}Mg (‰)
Starting material			11.48	46.00	19.39	23.12								0.008 ± 0.017
1900 °C														
R3-12	2.5	0	11.37	44.53	19.26	24.84	22.4	21.3	25.4	7.9	0.29			
R3-10	2.5	15	9.13	31.52	26.86	32.48	24.0	18.9	28.4	32.0	42.59	1.92×10^{-7}	6.02×10^{-7}	8.135 ± 0.007
R3-11	2.5	20	3.33	25.24	32.35	39.09	20.9	15.9	22.6	43.8	82.61	2.44×10^{-7}	5.42×10^{-7}	25.810 ± 0.020
R3-13	2.5	25	0.09	17.76	37.08	45.05	21.3	15.4	23.3	50.6	99.59	2.40×10^{-7}	5.25×10^{-7}	
R3-15	2.5	25	0.80	21.10	35.10	43.10	21.7	15.8	24.1	47.3	96.15	2.35×10^{-7}	4.97×10^{-7}	47.733 ± 0.023
R3-9	2.5	30	1.04	21.81	35.06	42.08	26.4	18.2	35.6	48.3	94.99	2.41×10^{-7}	5.13×10^{-7}	43.265 ± 0.017
1800 °C														
R-16	1.0	0	11.77	44.44	20.01	23.78	5.9	5.8	4.2	2.4	0.68			
R-14	1.0	30	7.03	29.63	29.03	34.31	5.8	5.0	4.1	31.7	59.11			
R-15	1.0	45	2.91	25.40	32.87	38.82	6.0	4.7	4.5	42.2	85.06			
R-17	1.0	60	0.09	18.49	37.39	44.03	6.0	4.2	4.4	50.0	99.62			
R-6	2.5	0	11.66	45.34	19.64	23.36	20.0	19.7	20.9	2.4	−0.27			0.130 ± 0.025
R-3	2.5	30	11.82	38.87	22.55	26.76	21.5	19.5	23.8	14.3	11.47	2.18×10^{-8}	1.36×10^{-7}	1.723 ± 0.009
R-2	2.5	60	10.07	33.58	25.72	30.63	22.8	18.9	26.3	26.2	33.86	3.52×10^{-8}	1.24×10^{-7}	5.494 ± 0.044
R-18	2.5	90	5.20	28.05	30.51	36.24	27.4	21.8	39.9	36.1	71.21	6.08×10^{-8}	1.41×10^{-7}	17.059 ± 0.032
R-4	2.5	90	4.61	27.45	31.07	36.87	20.6	16.3	22.2	38.3	74.94	4.77×10^{-8}	1.08×10^{-7}	18.681 ± 0.042
R3-14	2.5	100	3.12	26.13	31.76	38.98	23.5	17.4	27.6	40.9	83.41	5.38×10^{-8}	1.15×10^{-7}	25.372 ± 0.031
R2-1	2.5	105	0.19	19.91	36.53	43.38	21.7	15.6	24.2	49.2	99.12	5.82×10^{-8}	1.23×10^{-7}	69.148 ± 0.063
R-7	3.3	60	7.67	30.45	28.23	33.65	27.8	24.4	30.1	31.9	54.11	4.97×10^{-8}	1.35×10^{-7}	10.574 ± 0.044
R-13	6.0	0	11.64	45.48	19.58	23.31								≡0.000
R-8	6.0	30	11.94	40.59	21.69	25.77	87.5	83.4	171.9	11.1	7.02	2.39×10^{-8}	1.84×10^{-7}	0.935 ± 0.029
R-9	6.0	60	11.08	35.70	24.31	28.91	82.6	76.6	146.6	20.6	23.02	3.40×10^{-8}	1.50×10^{-7}	3.547 ± 0.027
R-11	6.0	90	9.16	32.36	26.78	31.70	91.3	80.0	190.4	27.8	42.23	4.97×10^{-8}	1.55×10^{-7}	7.689 ± 0.028
R2-4	6.0	120	4.92	28.11	30.57	36.40	88.5	75.5	176.6	37.0	72.82	6.22×10^{-8}	1.41×10^{-7}	18.867 ± 0.083
R2-5	6.0	180	0.06	18.69	37.47	43.79	90.4	72.5	186.0	49.8	99.73	6.00×10^{-8}	1.29×10^{-7}	
1700 °C														
R2-21	1.0	0	11.42	45.80	19.56	23.23	3.9	3.7	1.8	11.1	1.39			0.209 ± 0.044
R2-20	1.0	90	3.61	26.55	30.20	39.64	4.2	3.4	2.0	35.0	79.81			20.574 ± 0.044
R2-18	1.0	120	5.29	29.15	29.75	35.81	4.7	3.6	2.5	36.0	69.97			15.661 ± 0.097
R2-19	1.0	150	4.62	28.17	30.95	36.27	5.4	4.3	3.4	35.3	74.79			
R2-17	1.0	180	0.26	22.75	36.88	40.12	5.1	3.5	2.8	46.4	98.81			
R2-7	1.0	270	0.02	19.26	36.86	43.86	5.6	4.0	3.7	45.9	99.91			
R2-3	2.5	180	8.76	32.67	26.80	31.77	17.9	15.6	16.9	28.4	44.79	1.20×10^{-8}	3.51×10^{-8}	
R2-10	2.5	240	9.50	33.72	25.85	30.91	22.2	18.5	25.4	26.0	37.93	9.55×10^{-9}	3.03×10^{-8}	6.246 ± 0.091
R2-16	2.5	330	0.94	23.78	34.46	40.83	18.4	14.8	17.8	44.4	95.39	1.48×10^{-8}	2.96×10^{-8}	41.201 ± 0.051
R2-11	2.5	420	4.92	28.99	30.19	35.89	24.0	18.2	28.7	36.2	72.47	1.12×10^{-8}	2.48×10^{-8}	16.401 ± 0.050
R2-12	2.5	480	1.33	24.56	33.77	40.36	25.2	17.7	31.9	45.5	93.35	1.37×10^{-8}	2.80×10^{-8}	34.976 ± 0.116
R2-2	2.5	540	0.02	11.04	41.39	47.55	19.7	14.4	20.5	53.7	99.92	1.06×10^{-8}	2.52×10^{-8}	

(*continued on next page*)

Table 1 (*continued*)

Sample	Diam (mm)	Run time (min)	MgO (wt%)	SiO_2 (wt%)	Al_2O_3 (wt%)	CaO (wt%)	Init[a] area (mm^2)	Final[a] area (mm^2)	Init wt mg	% Mass loss	% Mg loss	J_{Mg}[a] ($mol\ cm^{-2}\ s^{-1}$)	J_{Si}[a] ($mol\ cm^{-2}\ s^{-1}$)	$\delta^{25}Mg$ (‰)
1600 °C														
R2-13	1.0	900	4.55	29.40	30.21	35.84	5.2	3.9	3.0	36.7	74.56			
R2-15	1.0	1200	5.24	30.16	29.53	35.11	5.9	4.9	4.3	34.9	70.03			
R2-14	1.0	1500	0.04	20.86	36.10	43.00	5.4	3.8	3.4	45.6	99.81			
R2-9	1.0	1800	0.02	16.29	39.28	44.41	6.0	4.1	4.4	50.0	99.91			
R2-8	1.0	2250	0.03	8.54	45.21	46.22	4.9	3.1	2.7	59.3	99.89			
R3-2	2.5	0	12.22	46.36	19.31	22.11	22.1	21.9	25.0	0.0	0.00			-0.105 ± 0.014
R3-1	2.5	1800	9.62	33.93	26.24	30.21	22.3	18.5	25.7	26.5	42.07	1.49×10^{-9}	4.16×10^{-9}	6.188 ± 0.006
R3-20	2.5	2400	6.43	31.01	29.11	33.45	22.2	17.6	25.6	34.0	65.10	1.76×10^{-9}	3.85×10^{-9}	12.337 ± 0.053
R3-21	2.5	2400	9.44	33.69	26.32	30.54	25.4	21.0	33.0	26.7	43.32	1.30×10^{-9}	3.56×10^{-9}	
R3-4	2.5	2700	4.60	30.84	30.20	34.36	20.6	16.7	22.5	33.3	75.93	1.69×10^{-9}	3.19×10^{-9}	19.861 ± 0.023
R3-7	2.5	2998	0.20	22.40	36.01	41.39	20.4	15.5	22.0	45.5	99.12	2.05×10^{-9}	3.88×10^{-9}	
R3-19	2.5	3000	6.70	31.34	28.86	33.11	25.1	19.6	31.7	32.8	63.31	1.51×10^{-9}	3.32×10^{-9}	11.887 ± 0.042
R3-18	2.5	3000	4.34	29.39	30.81	35.46	21.8	16.9	24.8	37.5	77.74	1.68×10^{-9}	3.32×10^{-9}	17.946 ± 0.023
R3-8	2.5	3600	1.65	26.73	33.21	38.40	21.2	16.1	23.7	41.4	92.15	1.64×10^{-9}	3.00×10^{-9}	32.359 ± 0.016
R3-5	2.5	4285	0.12	17.74	38.36	43.78	20.9	15.3	23.1	48.5	99.51	1.50×10^{-9}	3.07×10^{-9}	

[a] Estimated uncertainties are 20% for 1 mm diameter samples and 10% for larger samples. Because of the larger uncertainty, evaporation rates are not reported for 1 mm samples; the rates for larger samples are uncertain by ~10%, mostly because of uncertainty in surface areas.

nesses. Based on comparing the different calculations we made for the surface area of our samples, we estimate that the uncertainty in the surface area of the 2.5 and 6 mm samples is less than 10%. The surface areas for the 1 mm samples are more uncertain, and therefore we did not calculate an evaporation flux for these small samples.

3.2. Analytical methods

The major element composition of the starting materials and chips of the evaporation residues were measured using a JEOL JSM-5800LV scanning electron microscope (SEM) with an Oxford Link ISIS-300 energy dispersive microanalysis system (EDS). The microanalysis system was calibrated with a variety of pure oxides and minerals of known chemical composition. At least 20 spots were analyzed in each chip to check for homogeneity.

Splits of the starting materials and of the evaporation residues were crushed in a boron carbide mortar and pestle and then digested in high-purity 3:1 HF/HNO_3 at 70 °C. The Mg/Al ratio of most of these dissolved samples was also measured by plasma mass spectrometry (see below) as a further check on the fractionation of magnesium from aluminum, the latter being sufficiently refractory that its evaporation would have been negligible under the conditions of our experiments.

The dissolved samples were converted to 1 N nitric acid solutions by evaporating and redissolving two or more times in high-purity, double-distilled concentrated nitric acid, and the final solution was made by taking up the sample in 1 N nitric acid. One hundred microliters of this final sample solution, representing approximately one mg weight equivalent of sample and 1–50 μg magnesium, was put through a cation exchange column (2 mm ID by 240 mm) using approximately 1.2 ml of AG50W-X8 resin in a 1 N nitric acid medium to separate the magnesium. In the case of highly evaporated samples, the eluted magnesium had to be reprocessed through the cation-exchange chemistry to lower the Al/Mg (i.e., $Al/Mg < 0.05$; Galy et al., 2001). Aliquots of a few samples with already sufficiently low Al/Mg for isotopic analysis after the first column separation were reprocessed to test whether multiple passes through the cation exchange column affected the magnesium isotopic compositions (it did not). As a final step, a fraction of the purified magnesium solutions was diluted in ultrapure 3 wt% nitric acid to between 0.2 ppm and 0.5 ppm.

The magnesium isotopic composition of the starting materials and evaporation residues were measured using the Micromass Isoprobe multi-collector magnetic sector inductively coupled plasma mass spectrometer (MC-ICPMS) in the Isotope Geochemistry Laboratory (IGL) at the Field Museum. Sample solutions were introduced to the mass spectrometer using a CETAC Aridus desolvating nebulizer. The three isotopes of magnesium (^{24}Mg, ^{25}Mg and ^{26}Mg), as well as ^{27}Al were measured by static multicollection using four faraday collectors (using the L3, Axial, H4 and H6 collectors, respectively). Each measurement consisted of a 60 s on-peak blank measurement followed by a 200 s sample acquisition (comprising 20 cycles of 10 s each). Samples were typically run with ion currents for ^{24}Mg of $3.5–5 \times 10^{-11}$ A. Background ion currents on all collectors were typically less than 1×10^{-14} A. Isotope ratio values were determined using sample-standard bracketing using 0.2–0.5 ppm solutions of either NIST standard reference material SRM-980 (December 2002 to March 2004) or the magnesium isotope standard DSM3 (Galy et al., 2003) (October 2004 through August 2006). Each isotope ratio reported represents the mean of two to five individual measurements. Data are reported relative to the isotopic composition of sample B133 R-13, a 6 mm sample run at 1800 °C for "zero time" (i.e., the sample was heated in the furnace only long enough for it to reach 1800 °C, whereupon the sample was immediately quenched). This sample, which was determined to have the same isotopic composition as the starting material (sample R-10), was run in every analytical session. Galy et al. (2003) showed that SRM-980 is isotopically heterogeneous from batch to batch. However all of our earlier analyses used the same batch of this standard. Since B133 R-13 was measured during every session, the offset between our SRM-980 batch and DSM-3, could be determined precisely. Relative to DSM-3, our batch of SRM-980 had δ^{25}Mg = −2.488‰ and δ^{26}Mg = −4.792‰. Fifty measurements of B133 R-13 made over more than three and half years indicate that our long-term 2σ precision for δ^{25}Mg is 0.025‰ and for δ^{26}Mg is 0.047‰.

A detailed review of the isotopic data that had been obtained after the entire set of samples had been measured revealed that some of the MC-ICPMS sessions had a problem in that on some days the MC-ICPMS behaved as if it had a memory. During these sessions, when running a sample with a fractionated magnesium isotopic composition the isotope ratios of ^{25}Mg/^{24}Mg and ^{26}Mg/^{24}Mg would drift upwards during the 20 cycles of a sample acquisition; when the standard was run after such a fractionated sample, the isotope ratios would drift downward. This effect persisted despite the fact that a 1 M HNO_3 blank solution with no magnesium was run between the samples and standards and the intensities on the faraday cups were at background levels. We do not have an explanation for this "memory-like" behavior, but it largely disappeared following an instrumental upgrade in early 2004, when the sample interface/cone arrangement was changed. We rejected all data on days when this behavior was observed and re-ran these samples under optimum conditions in 2006. A comparison of samples run under "memory effect" conditions with those run under optimum conditions showed a small shift in data toward higher delta values, 0.0106 ± 0.0027 per ‰ for δ^{25}Mg and 0.0120 ± 0.0024 per ‰ for δ^{26}Mg. This indicates that the "memory effect" had only a small effect on the data, and only on the most highly fractionated samples. In the end, only one sample, R2-16, had insufficient solution remaining and no fresh sample to dissolve and thus was not able to be run under optimal conditions. The data reported in Table 1, apart from R2-16, are from sessions when the MC-ICPMS was most stable and for solutions in which the Al/Mg ratios were at an acceptably low value of <0.05.

The Al/Mg ratios of most of the dissolved samples (but not yet chemically processed by ion exchange) were measured by static multicollection on the IGL Isoprobe. Calibration was achieved through the use of a series of standards prepared from purified Mg and Al elemental solutions, spanning a range of Al/Mg ratios from 1 to 100. Accuracy was checked via the analysis of USGS rock standard AGV-1, which agreed to within 5% of the certified value. A comparison of the chemical compositions measured by the scanning electron microscope and those done by ICPMS is given in Fig. 1, which shows that the two methods give similar results within uncertainties. The chemical compositions and calculated losses of magnesium and silicon by evaporation listed in Table 1 are those measured using the SEM-EDS at the University of Chicago.

4. RESULTS

The elemental and isotopic compositions of starting materials and evaporation residues, along with the experimental conditions, are listed in Table 1. These data were used to determine the trajectory in composition space of the evaporation residues, the kinetics of magnesium and silicon evaporating into vacuum as a function of temperature, and the kinetic isotopic fractionation factor for magnesium as a function of temperature.

4.1. Evaporation kinetics

The evaporation rate of silicon and magnesium in vacuum experiments with Type B CAI-like liquids run at T = 1600, 1700, 1800, and 1900 °C is shown in Fig. 2. Calcium and aluminum are sufficiently refractory that they do not experience any significant loss by evaporation until virtually all of the magnesium has evaporated. It should be kept in mind that the rates shown in Fig. 2 are for vacuum evaporation, and thus significantly lower than what would be the case for the more realistic natural conditions when

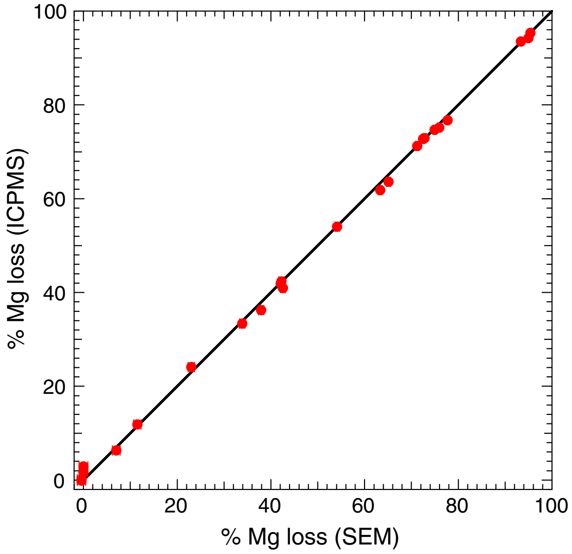

Fig. 1. Comparison of % Mg loss based on Al/Mg ratios measured by energy dispersive X-ray microanalysis on an SEM with those measured by MC-ICPMS on solutions of the same sample.

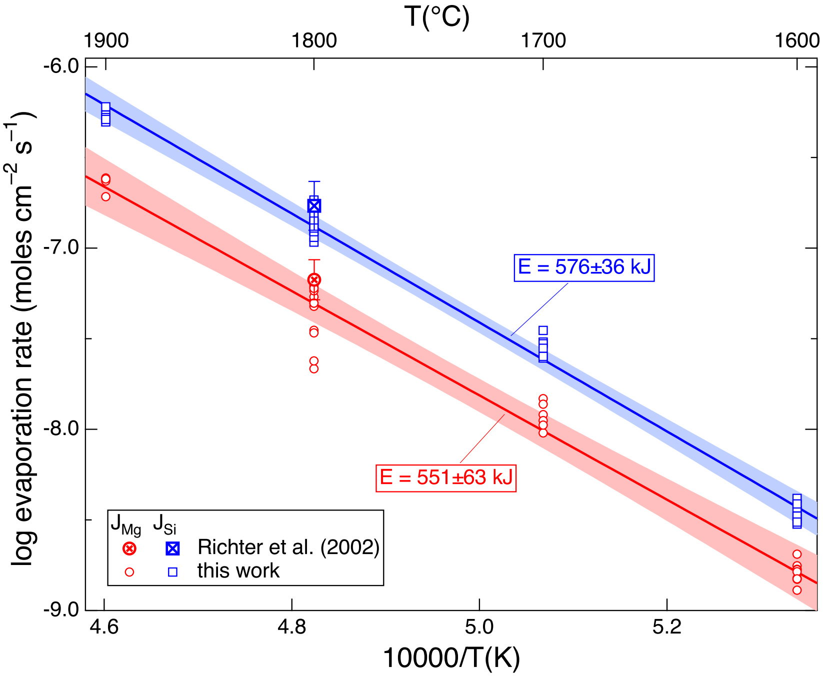

Fig. 2. Vacuum evaporation rates of silicon and magnesium from a Type B CAI-like liquid as a function of temperature. Only the 2.5 mm and 6 mm samples are plotted. The evaporation rates of the 1 mm samples are not included because of larger uncertainties in the effective surface area of the smaller samples. The fits to the data correspond to $J = J_0 e^{-E/RT}$ with $J_0 = 3.81 \times 10^6$ mol cm^{-2} s^{-1}, $E = 551 \pm 63$ kJ mol^{-1} for magnesium; $J_0 = 4.17 \times 10^7$ mol cm^{-2} s^{-1}, $E = 576 \pm 36$ kJ mol^{-1} for silicon. All uncertainties and error envelopes are 2σ, and are based on the scatter of the data about the regression line. The effect of uncertainties in the surface area of samples on the reported evaporation rates (see text) is smaller than that implied by the scatter of the data about the best fitting regression line. The average evaporation rates of magnesium and silicon measured at 1800 °C by Richter et al. (2002) are shown for comparison, but were not included in the regression.

the Type B CAIs would have been surrounded by a finite pressure of hydrogen gas (Richter et al., 2002). A reasonable and testable assumption is that the effect of hydrogen on the evaporation kinetics is captured by its effect on the saturation vapor pressure, a quantity that can be calculated from thermodynamic data in the manner described in Grossman et al. (2000). This being the case, the key parameter for determining the evaporation kinetics regardless of the pressure of surrounding hydrogen gas is the evaporation coefficient as defined by Eqs. (1) and (2). Fig. 3 is a plot of the evaporation coefficients for silicon and magnesium corresponding to the evaporation rates shown in Fig. 2, and a significant dependence of the evaporation coefficients on temperature is obvious. This temperature dependence of the evaporation coefficients needs to be taken into account when using Eq. (1) or (2) to calculate the evaporation kinetics. Also shown in Fig. 3 are evaporation coefficients for silicon and magnesium from experiments reported by Richter et al. (2002) involving Type B CAI-like compositions evaporated in 2×10^{-4} bars of hydrogen at $T = 1500$ °C. Even though the evaporation rate in 2×10^{-4} bars of hydrogen is about two orders of magnitude faster than in vacuum (see Fig. 12 in Richter et al., 2002), the evaporation coefficients for evaporations done in hydrogen fall on the trend with temperature of the vacuum data. This implies that reasonably accurate evaporation rates can be obtained for both vacuum and finite hydrogen pressure conditions using Eq. (2) with calculated saturation vapor pressures and the temperature dependent evaporations coefficients shown in Fig. 3. The effect of finite hydrogen pressure on the evaporation rate is entirely due to the dependence of the saturation vapor pressures on the hydrogen pressure in the surrounding gas.

4.2. Elemental fractionations

Published reports (e.g., Grossman et al., 2000; Richter et al., 2002; Grossman et al., 2002; Grossman and Fedkin, 2003) have used different ratios of the evaporation coefficients of magnesium and silicon when calculating the relative evaporation rates of these components. The evaporation coefficients plotted in Fig. 3 are not sufficiently precise to resolve whether the coefficients for silicon and magnesium are the same or different. A far more sensitive approach for determining the ratio of the evaporation coefficients is to compare the composition trajectories of evaporation residues with trajectories calculated for particular choices of the evaporation coefficients.

Evaporation trajectories of evaporation residues are calculated from the following conservation equations.

$$\frac{dM_{Mg}}{dt} = -J_{Mg}A \tag{8}$$

where M_{Mg} is the total moles of magnesium in the evaporation residue, J_{Mg} is the evaporation rate (mol cm^{-2} s^{-1}) of magnesium appropriate for the composition of the substrate, and A is the surface area of the evaporating material. J_{Mg} is calculated using Eq. (2) with the saturation vapor

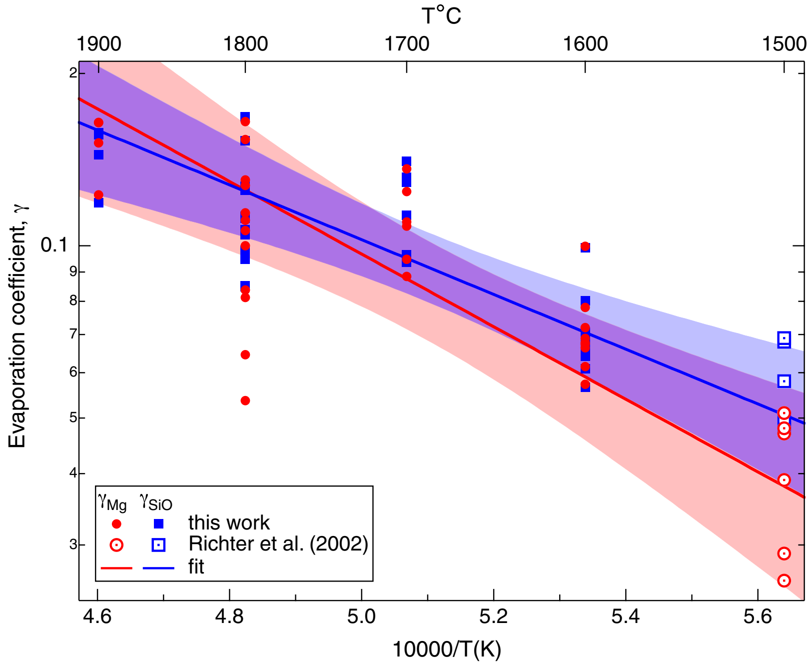

Fig. 3. Evaporation coefficients as a function of temperature calculated from the evaporation rates shown in Fig. 2 and saturation vapor pressures of Mg and SiO in equilibrium with the composition of the molten condensed phase in the manner discussed in Grossman et al. (2000). Also shown are the evaporation coefficients for silicon and magnesium reported by Richter et al. (2002) for experiments involving similar liquids evaporated at $T = 1500$ °C and a surrounding hydrogen pressure of 1.87×10^{-4} bars. The combined vacuum and finite hydrogen pressure data are fit by the functional form $\gamma = \gamma_0 e^{-E/RT}$ with $\gamma_0 = 25.3$, $E = 92 \pm 37$ kJ mol^{-1} for γ_{Si}; $\gamma_0 = 143$, $E = 121 \pm 53$ kJ mol^{-1} for γ_{Mg}. All uncertainties and error envelopes are 2σ, and are based on the scatter of the data about the regression lines.

pressure $P_{Mg,sat}$ calculated in the manner described in Grossman et al. (2000). The evolution of the total moles of silicon in the evaporation residue is given by a similar relationship:

$$\frac{dM_{Si}}{dt} = -J_{Si}A. \tag{9}$$

We now use Eq. (3) to relate the silicon evaporation rate to that of magnesium, which we rearrange as

$$J_{Si(t)} = J_{Mg(t)} \frac{\gamma_{Si} P_{SiO,sat}}{\gamma_{Mg} P_{Mg,sat}} \sqrt{\frac{m_{Mg}}{m_{SiO}}}. \tag{10}$$

Eqs. (8)–(10) can be advanced in time to yield $M_{Si(t)}$ and $M_{Mg(t)}$ that, together with the fact that the CaO and Al_2O_3 components do not evaporate, define a calculated trajectory in composition space of the evaporation residues. The thermodynamic model of Berman (1983) is used for calculating the activity of MgO and SiO_2 in the evolving condensed phase and the corresponding saturation vapor pressures of Mg and SiO are calculated as described in Grossman et al. (2000). Ignoring small effects due to isotopic fractionation, the mass of the main gas species containing magnesium and silicon are $m_{Mg} = 24.3$ and $m_{SiO} = 44.1$. The value of γ_{Si}/γ_{Mg} for the evaporation of silicon and magnesium from a Type B CAI-like liquid at a given temperature is then determined by the value of this ratio that produces the best fit between the measured and calculated compositions of evaporation residues.

Fig. 4 compares the MgO and SiO_2 composition of vacuum evaporation residues from experiments run for various lengths of time at 1600, 1700, 1800, and 1900 °C to calculated composition trajectories for the two choices of γ_{Si}/γ_{Mg}. Fig. 4a shows that the trajectory in MgO–SiO_2 space of the 1600 °C evaporation residues is fit reasonably well by a calculation using a ratio for the evaporation rates of Mg and SiO equal to the ratio of their respective saturation vapor pressures, implying that $\gamma_{Mg}/\gamma_{Si} = \sqrt{m_{Mg}/m_{SiO}} = 0.74$, the value used by Grossman et al. (2000). Note however, that this ratio of the evaporation coefficients does not fit the higher temperature data. Fig. 4b shows that the 1800 °C trajectory can be fit reasonably well assuming $\gamma_{Mg}/\gamma_{Si} = 1$ (a value used by Richter et al., 2002) rather than 0.74. The separately measured evaporation coefficients for magnesium and silicon (Fig. 3) are not sufficiently precise to resolve any differences between them. By using calculated trajectories to fit the MgO and SiO_2 composition of evaporation residues from experiments run at $T = 1600$ and 1800 °C we were able to resolve that the evaporation coefficient of magnesium actually increased about 25% more than that of silicon between $T = 1600$ and 1800 °C. This result shows that there is no inconsistency in Grossman et al. (2000) and Richter et al. (2002) having used different values for γ_{Mg}/γ_{Si}, given different evaporation temperatures for the samples in two studies and the effect of this temperature difference on γ_{Mg}/γ_{Si}.

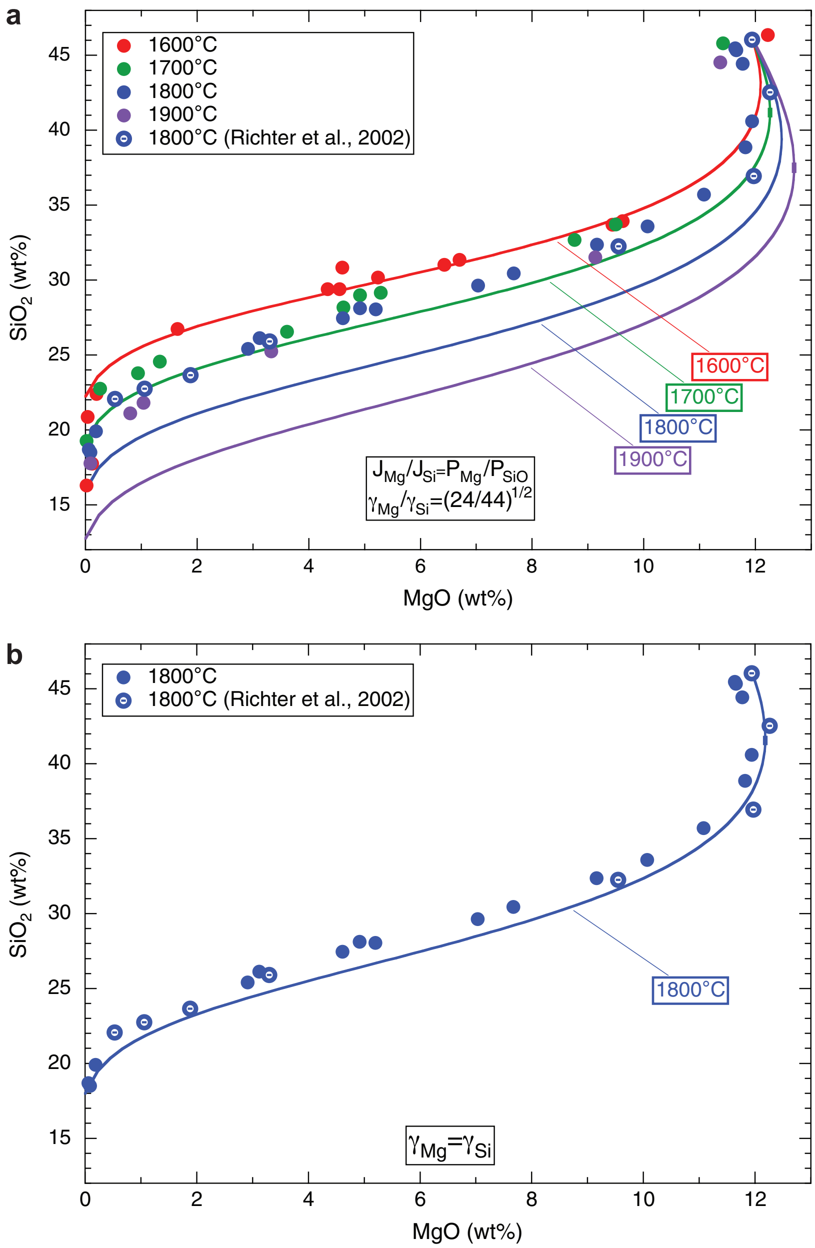

Fig. 4. Trajectories in SiO_2–MgO composition space of residues evaporated at various temperatures compared to calculated trajectories. The different sets of experiments shown by distinct symbols had slightly different starting compositions and for simplicity we only show calculated trajectories for the starting composition used by Richter et al. (2002). Trajectories corresponding to the other starting composition involve a simple translation of the trajectory in wt% MgO so that the trajectory falls on the relevant starting composition. (a) Composition of the evaporation residues compared to trajectories calculated under the assumption that $J_{Mg}/J_{Si} = P_{Mg}/P_{SiO}$. Only the trajectory for $T = 1600$ °C shows a reasonable fit to the corresponding measured compositions. (b) Composition of residues from $T = 1800$ °C experiments compared to a trajectory for $T = 1800$ °C now calculated assuming that the evaporation coefficients of magnesium and silicon are equal (i.e., $\gamma_{Mg} = \gamma_{Si}$ and thus $J_{Mg}/J_{Si} = (P_{Mg}/P_{SiO}) \times \sqrt{44/24}$).

4.3. Isotopic fractionation

Fig. 5 compares the magnesium isotopic fractionation of evaporated Type B CAI-like samples measured by MC-ICPMS and those reported earlier by Richter et al. (2002) and Mendybaev et al. (2003), which were measured using the modified AEI IM-20 ion microprobe at the University of Chicago. Also shown in Fig. 5 are two calculated Rayleigh fractionation curves for the magnesium isotopic fractionation as a function of the fraction of magnesium evaporated, assuming in one case that the kinetic fractionation factor for the magnesium isotopes is equal to the inverse square root of the mass of the isotopes (i.e., $\alpha = \sqrt{24/25} = 0.97980$) and in the other case that $\alpha = 0.98704$ derived from the best fit to our new data. Both the new high-precision data and the older data show

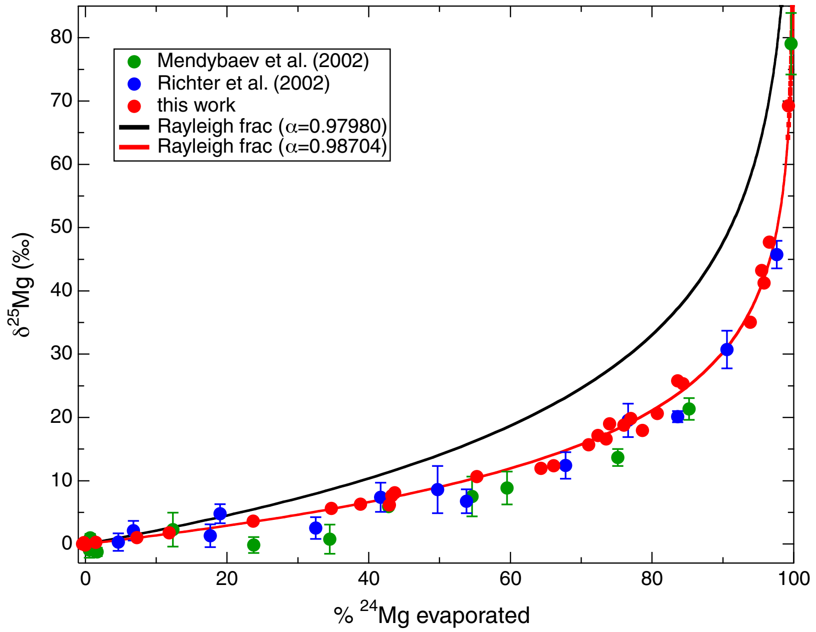

Fig. 5. Magnesium isotopic composition of evaporation residues relative to the Type B CAI-like starting material, plotted as a function of % ^{24}Mg evaporated. $\delta^{25}\mathrm{Mg} = 1000 \times \{(^{25}\mathrm{Mg}/^{24}\mathrm{Mg})_{\mathrm{sample}}/(^{25}\mathrm{Mg}/^{24}\mathrm{Mg})_{\mathrm{standard}} - 1\}$. 2σ uncertainties are plotted, but they are smaller than the symbols for most of the new data reported in this work. The continuous curves were calculated using the Rayleigh equation Eq. (7).

isotopic fractionations as a function of magnesium evaporated that are significantly less than those calculated using $\alpha = \sqrt{24/25}$. There are various differences worth noting between the MC-ICPMS isotopic measurements and those made earlier using the Chicago ion microprobe. The MC-ICPMS measurements are more precise by about a factor of ten and tend to show more isotopic fractionation for a given amount of magnesium evaporated than the ion probe data. The magnesium isotopic composition of eight of the evaporation residues listed in Table 1 were measured by both methods. Comparing the results shows even more clearly that there is a systematic difference with the ion probe isotopic measurements being systematically less fractionated. The isotopic measurements made by MC-ICPMS are the more likely to be correct, not because they are more precise, but because they were done on purified magnesium solutions, thus avoiding possible artifacts due to matrix effects that in the case of the ion probed samples could be quite significant because of the large range of magnesium content of the various evaporation residues and the correlation between magnesium content and isotopic fractionation.

An intriguing aspect of the data shown in Fig. 5 is that the MC-ICPMS data scatter around the best fitting fractionation curve by an amount that is significantly larger than the 2σ uncertainty of each data point. This can be seen more clearly in Fig. 6, which is a plot of the same data now using $\ln(R/R_0)$ versus $-\ln(f_{24\mathrm{Mg}})$, where $R = {}^{25}\mathrm{Mg}/{}^{24}\mathrm{Mg}$ of a sample, R_0 is this ratio in the starting material, and $f_{24\mathrm{Mg}}$ is the fraction of ^{24}Mg remaining in the residue. The advantage of plotting the data in this way can be seen by taking the natural logarithm of both sides of Eq. (7) applied to $^{25}\mathrm{Mg}/^{24}\mathrm{Mg}$ with the result

$$\ln\left(\frac{R}{R_0}\right) = -(1-\alpha_{\mathrm{Mg}})\ln(f_{^{24}\mathrm{Mg}}), \tag{11}$$

The magnesium isotopic data plotted in the manner of Fig. 6 should, if the process is governed by Rayleigh fractionation, fall on a straight line with slope $1 - \alpha_{\mathrm{Mg}}$. An unexpected result is that the departures of the data points from the best fitting line through the data in Fig. 6 are correlated with the evaporation temperature. Fig. 7 is a plot of the magnesium isotopic data of the 2.5 mm samples listed in Table 1 using different symbols to distinguish the evaporation temperature along with the best fitting line through the data for each separate temperature. A well-resolved dependence of the isotopic fractionation factor on temperature is seen, and the scatter of the data around the best fitting line for each temperature is now consistent with the analytical uncertainty of the data. The fact that the data from samples of a common size evaporated to very different degrees at a common temperature fall so closely along a straight line has the further implication that the kinetic isotopic fractionation factor for magnesium evaporating from a CMAS liquid is remarkably insensitive to the MgO content of the melt.

Another possible source of the scatter of the magnesium isotopic data shown in Fig. 6 is that the isotopic fractionation factor is related to sample size. Samples ranging in size from 1 mm to 6 mm were run as a way of assessing the degree to which the results might have been affected by recondensation, which will have been greatest for the larger samples. Fig. 8 is the same type of plot as Fig. 7 but now showing the magnesium isotopic fractionation of samples with nominal diameters of 6 mm and 2.5 mm (see Table 1 for their actual surface areas) that were evaporated

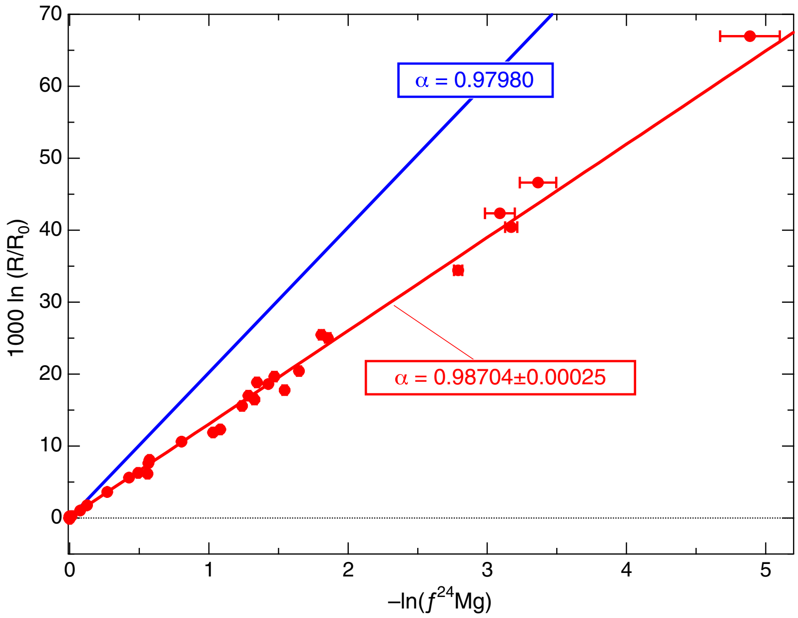

Fig. 6. Magnesium isotopic composition of the evaporation residues listed in Table 1 plotted as $1000 \times \ln(R/R_0)$ versus $-\ln f^{24}$Mg where f^{24}Mg is the fraction of ^{24}Mg remaining in the residue and $R = (^{24}\mathrm{Mg}/^{25}\mathrm{Mg})_{\mathrm{sample}}$, $R_0 = (^{24}\mathrm{Mg}/^{25}\mathrm{Mg})_{\mathrm{standard}}$. The 2σ error bars for the isotopic composition are smaller than the symbols used to plot the data. When isotopic compositions are plotted in this way, the data points will fall along a line of slope $1000 \times (1 - \alpha)$ if the process is Rayleigh fractionation (see Eq. (7)) and the kinetic isotope fractionation factor α is independent of the composition of the condensed phase. The red line is an error-weighted best fit (Williamson, 1968) through the data and corresponds to $\alpha = 0.98704$. The dashed line corresponds to the fractionation calculated using Eq. (7) assuming $\alpha = \sqrt{24/25} = 0.97980$. (For interpretation of the references to color in this figure legend, the reader is referred to the web version of this paper.)

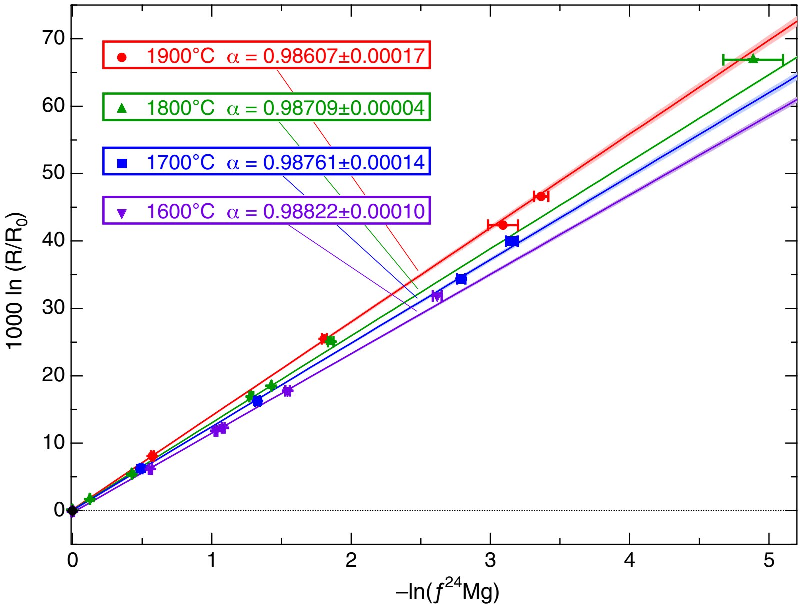

Fig. 7. Same as Fig. 6 except that now only the 2.5 mm samples from Table 1 are plotted and the temperature at which the residues were evaporated is now indicated by different symbols. Error-weighted best fits (Williamson, 1968) were made to the data from each temperature and these show that the kinetic isotope fractionation factors have a well-resolved dependence on the evaporation temperature. The shaded area around each line indicate the 2σ error bounds from the weighted regression.

at 1800 °C. Best fitting lines through the data for each sample size show that the larger samples are slightly more fractionated as a function of the amount of magnesium evaporated. This dependence on size is as expected for recondensation in a system of finite gas conductance, where with decreasing G^*, which is inversely proportional to sur-

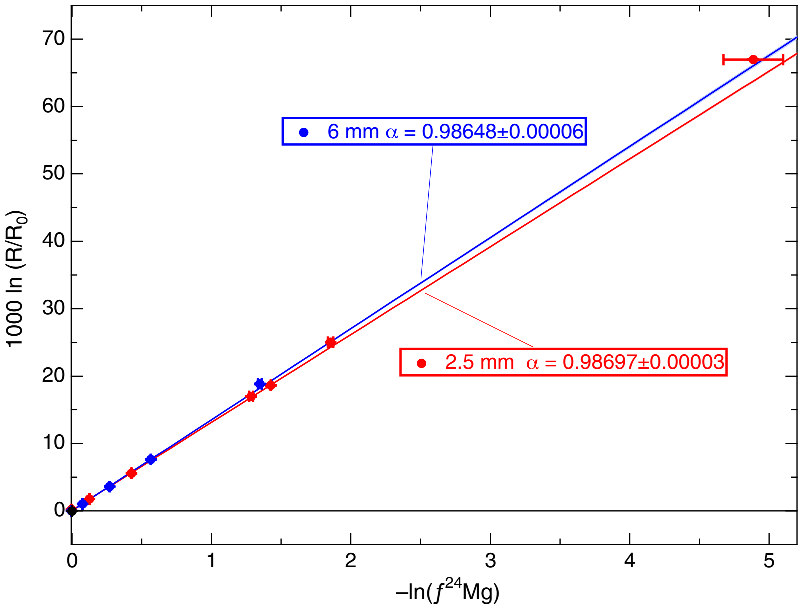

Fig. 8. Same type of plot as Fig. 6 except that now only data from the $T = 1800$ °C evaporation experiments are plotted. Different symbols are used to distinguish the nominally 6 mm samples from the 2.5 mm samples listed in Table 1 and show a slightly increased fractionation for the larger samples. The kinetic fractionation factor α corresponding to the best fitting line through the data for each sample size separately is indicated.

face area, the isotopic fractionation increases as the fractionation factor shifts towards the inverse square root of the mass of the evaporating species (see Eq. (A.12); Figs. A1 and A2 in Appendix A). We found no resolvable difference in the magnesium isotopic fractionation of 1 mm and 2.5 mm samples evaporated at 1700 °C (Fig. 9) implying that for samples of this size, recondensation effects were negligible.

5. SUMMARY AND DISCUSSION

The main motivation for the present study was to experimentally determine the appropriate kinetic isotope fractionation factor to use in connection with magnesium evaporating from Type B CAI-like liquids. The first thing to note is that all reported experimental determinations of the fractionation factors for ^{25}Mg from ^{24}Mg in molten sil-

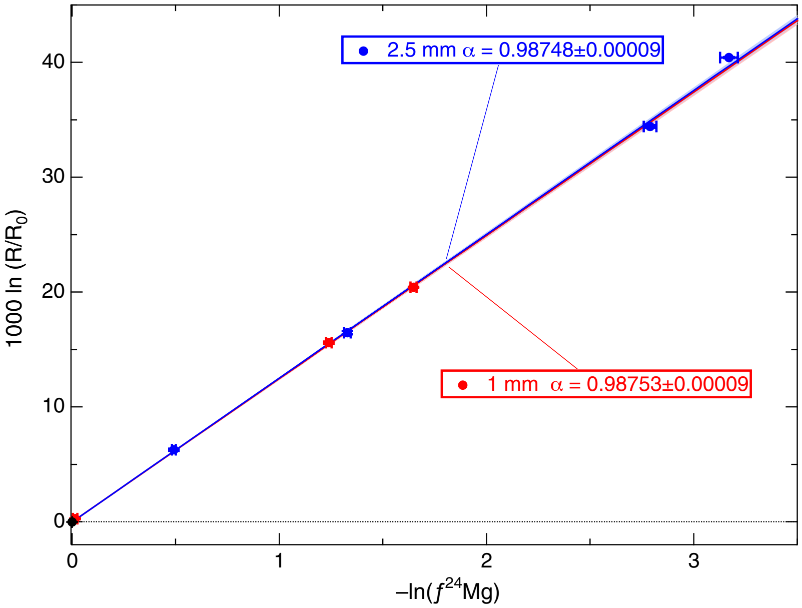

Fig. 9. Same as Fig. 6 except that now only data from the $T = 1700$ °C evaporation experiments are plotted. Different symbols are used to distinguish the nominally 2.5 mm samples from the 1.0 mm samples listed in Table 1. In this case there is no resolvable dependence of the kinetic isotope fractionation factor on sample size, which we interpret to mean that recondensation is negligible for samples of this size.

icate evaporation residues of various types (Davis et al., 1990 for molten Mg_2SiO_4; Wang et al., 2001 for a mixture of major oxides in solar proportions; Richter et al., 2002 for Type B CAI-like compositions) are significantly closer to one (or equivalently that $1-\alpha_{Mg}$ is significantly smaller) than the often assumed value of $\alpha_{Mg}=\sqrt{24/25}$. Whereas in the past there may have been some concern that this difference between the measured α_{Mg} and $\sqrt{24/25}$ reflected an experimental artifact due to recondensation, we have shown that the effect of recondensation in a finite conductance vacuum furnace would, if anything, tend to shift α_{Mg} towards rather than away from $\sqrt{24/25}$ (Figs. A1 and A2). Using samples of different size, we showed (see Fig. 8) that the largest samples (6mm nominal diameter) were indeed slightly more enriched in ^{25}Mg in a way that reflected the predicted effect of recondensation. We found no measurable difference in the Mg isotopic fractionation as a function of size between 1 mm and 2.5 mm samples (Fig. 9), which we take as evidence that the effects of recondensation are negligible for experimental samples in this size range.

An important feature of the kinetic fractionation factors that only became apparent because of the high precision of the new isotopic measurements is the distinct tendency of $1-\alpha_{Mg}$ to increase with temperature (Fig. 7). Similar temperature effects have been reported for the isotopic fractionation factor for magnesium evaporation from solid forsterite (Yamada et al., 2006). The systematic temperature dependence of α_{Mg} turns out to be very relevant to the interpretation of the isotopic fractionation of the Type B CAIs because the peak temperatures they experienced ($T\sim 1400$ °C, Stolper and Paque, 1986; Mendybaev et al., 2006) are lower than the temperature of laboratory evaporation experiments. Assigning a realistic value for the magnesium isotopic fractionation factor of partially molten Type B CAI precursors requires extrapolating the laboratory data to temperatures between their peak temperature of about $T=1400$ °C and the solidus at about 1250 °C. Fig. 10 shows our new determinations of the kinetic isotope fractionation factor for magnesium together with values from the literature plotted as a function of the temperature at which they were evaporated.

The literature values plotted in Fig. 10 are somewhat different from those in a similar figure shown in Richter et al. (2005). Each α value was obtained from a regression of $\ln(R/R_0)$ versus $-\ln(f_{24Mg})$, forced through the origin. In each case, a weighted regression (Williamson, 1968) and a simple linear regression (which assumes that all data points only have uncertainty in $\ln(f_{24Mg})$ and all have the same uncertainty) were calculated. Some regressions are well-described by Williamson (1968) fit, having low χ^2 values, whereas others scatter by more that the errors on individual data points would have suggested. For the latter cases, the uncertainty in slope from the simple linear regression was adopted. The reason for the scatter in the data from the lit-

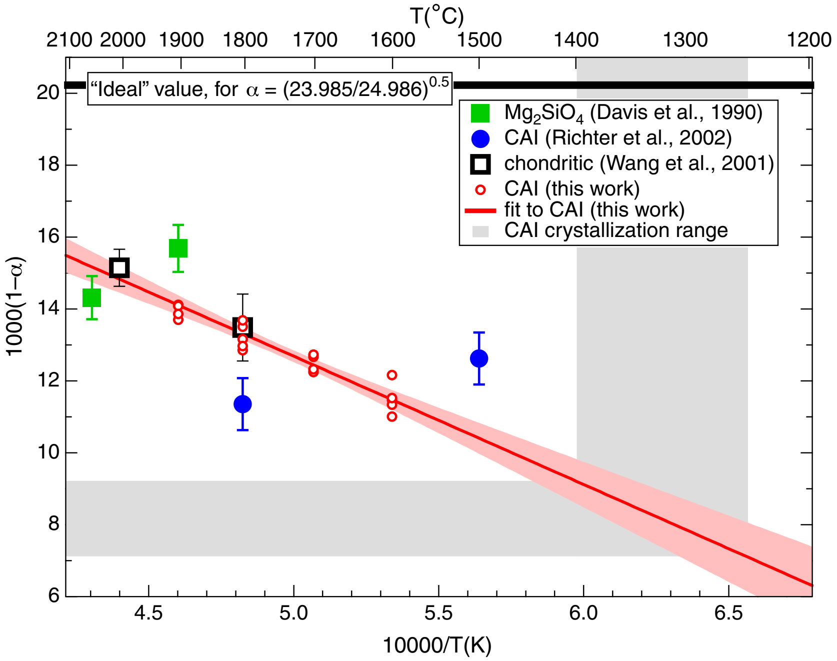

Fig. 10. Diagram showing the temperature dependence of the kinetic isotope fractionation factor for magnesium using data from the present study together with earlier data for molten forsterite and a melt with solar proportions of the major oxides. A simple linear regression of kinetic isotope fractionation factor vs. reciprocal temperature was calculated for the new vacuum evaporation experiments on CAI compositions, where the uncertainty in the fit is derived from the scatter of the data about the line; the error bounds shown are 2σ. The kinetic fractionation factor plotted at 1500 °C is from Richter et al. (2002) for 2.5 mm Type B CAI-like samples evaporated in 1.87×10^{-4} bars H_2; the one plotted at 1800 °C from the same paper is for 2.5 mm Type B CAI-like samples evaporated in vacuum. Shading is used to indicate the temperature interval relevant for calculating evaporation effects of partially molten Type B CAIs, along with extrapolations of $1000\times(1-\alpha)$ into this temperature range. The extrapolation shows that the Rayleigh fractionation exponent $(1-\alpha)$ in the temperature range of partially molten Type B CAI compositions is less than half that corresponding to $\alpha=\sqrt{24/25}=0.9798$ (shown by the line at $1000\times(1-\alpha)=20.2$).

erature is likely uncorrected matrix effects in the ion microprobe analysis: the Wang et al. (2001) and the 1500 °C Richter et al. (2002) samples were chemically heterogeneous because they crystallized when they were cooled from evaporation run temperature. The literature data alone only show a weak correlation with temperature in Fig. 10; it is only in the higher precision, matrix-effect-free new data collected by MC-ICPMS that the temperature effect is readily apparent.

The conclusion to be drawn from Fig. 10 is that the kinetic isotopic fractionation for magnesium evaporating from a partially molten Type B CAI-like liquid in the temperature range 1400–1250 °C will have $\alpha_{Mg} = 0.991$–0.993 (with an uncertainty of about ±0.001) rather than the often used value of $\alpha_{Mg} = \sqrt{24/25} = 0.9798$. The difference between these two values for the kinetic isotope fractionation factor of magnesium will have a large effect on the calculated amount of magnesium that must have evaporated in order to account for a given degree of magnesium isotopic fractionation, and a similarly large effect on estimates of the composition of the precursors of isotopically fractionated Type B CAIs. We illustrate this with reference to the Simon et al. (2004) recent effort to calculate the precursor composition of a set of Type B CAIs with known magnesium isotopic composition. Table 2 compares the amount of magnesium evaporated from the precursors as calculated by Simon et al. (2004) using $\alpha_{Mg} = \sqrt{24/25} = 0.9798$ to our estimate using the experimentally derived value of $\alpha_{Mg} = 0.991$. We believe that Simon et al. (2004) underestimated the fraction of magnesium evaporated by a factor of about two. We have not calculated revised estimates for the evaporated silicon for the Type B CAIs listed in Table 2 because we do not yet have a well-determined value for the silicon kinetic isotope fractionation factor, but studies to determine this are underway (see Janney et al., 2005).

We should emphasize that the kinetic isotope fractionation factors reported here apply to evaporations in the limit $P_i/P_{i,\mathrm{sat}} \ll 1$ (i.e., no recondensation) and situations where diffusion is sufficiently fast to maintain chemical homogeneity of the condensed phase. Richter (2004) used model calculations to explore the range of conditions when recondensation and chemical gradients will significantly affect the isotopic fractionation of evaporation residues and concluded that the Type B CAIs evaporated under conditions where the kinetic isotope fractionation factors reported here apply.

Table 2
Estimates of the amount of magnesium that must have evaporated to account for the measured magnesium isotopic composition of the Type B CAIs

Sample	Type	F_{Mg}[a] (‰ amu^{-1})	% Mg evap. $\alpha = 0.97978$[b]	% Mg evap. $\alpha = 0.991$[c]
F2 (TS65)	B2	6.12	26.0	49.2
E107	B2	1.99	9.4	19.9
3537-1	B1	3.26	14.9	30.4
TS33	B1	4.01	18.0	35.9
TS34	B1	5.63	24.2	46.4
Golfball	B	1.61	7.7	16.4

[a] $F_{Mg} \equiv 1000 \times \{(^{N}\mathrm{Mg}/^{24}\mathrm{Mg})_{\mathrm{sample}}/(^{N}\mathrm{Mg}/^{24}\mathrm{Mg})_{\mathrm{standard}} - 1\}/(N-24)$, averaged for $N = 25$ and 26.

[b] The value of α used by Simon et al. (2004).

[c] The value of α obtained by extrapolating Fig. 10 to 1400 °C.

The main conclusions of the present study regarding the evaporation kinetics of magnesium and silicon from Type B CAI-like liquids are:

1. The vacuum evaporation rates J_{Si} and J_{Mg} can be calculated using a parameterization *of the form* $J = J_o e^{-E/RT}$ with $J_o = 3.81 \times 10^6$ mol cm^{-2} s^{-1}, $E = 551 \pm 63$ kJ mol^{-1} for magnesium; $J_o = 4.17 \times 10^7$ mol cm^{-2} s^{-1}, $E = 576 \pm 36$ kJ mol^{-1} for silicon.
2. Evaporation rates of silicon and magnesium as a function of temperature and finite surrounding pressure can be calculated using Eq. (2) with the evaporation coefficients as a function of temperature shown in Fig. 3 (parameterized as $\gamma = \gamma_o e^{-E/RT}$ with $\gamma_o = 25.3$, $E = 92 \pm 37$ kJ mol^{-1} for γ_{Si}; $\gamma_o = 143$, E=121 ± 53 kJ mol^{-1} for γ_{Mg}) together with the saturation vapor pressures of the dominant gas species calculated using Berman's (1983) thermodynamic model for the CMAS liquids in the manner described in Grossman et al. (2000).

The main conclusions regarding the kinetic isotope fractionation of magnesium evaporating from a Type B CAI-like silicate liquid are:

1. The magnesium isotopic fractionation of residues of similar size, evaporated to different degrees at a given temperature, fall within error on a Rayleigh fractionation curve as given by Eq. (7), implying that the isotopic fractionation factor is effectively independent of the amount of magnesium (i.e., the activity of magnesium) in the silicate liquid.
2. The magnesium isotopic fractionation of residues of similar size evaporated at different temperatures imply, as we show in Fig. 7, that the kinetic fractionation factor is significantly temperature dependent, becoming larger (i.e., less fractionating) with decreasing temperature.
3. The magnesium isotopic fractionation of residues of different size evaporated at the same temperature showed that the largest samples were slightly more fractionated (Fig. 8), which agrees with our derivation for the effect of sample size on recondensation and the effect of this recondensation on the isotopic fractionation in system of finite gas conductance (Figs. A1 and A2 in Appendix A).
4. Taking the effect of temperature into account results in an estimate for the kinetic isotope fractionation factor for magnesium evaporating from a Type B CAI-like liquid in the temperature range where Type B CAI-like compositions are partially molten (~1400–1250 °C) of $\alpha_{Mg} = 0.991$–0.993 (Fig. 10). Adopting this value for the kinetic isotope fractionation factor for magnesium results in estimates of the amount of magnesium evaporated for a given

degree if magnesium isotopic fractionation that are about a factor of two larger than calculated using $\alpha_{\mathrm{Mg}} = \sqrt{24/25} = 0.9798$.

In closing we should emphasize that the reason laboratory experiments are so critical for defining the evaporation coefficients, γ, and the kinetic isotope fractionation factors, α, for a silicate liquid is that there is not yet a theoretical basis for determining these quantities from first principles. From the theoretical point of view, what is needed is an understanding of what determines that the evaporation coefficients from a silicate liquid are so much less than one, and in the case of isotopes, why the ratio of their evaporation coefficients is different from one. Wang et al. (1999) have suggested that the explanation might involve the dominant gas species being different from those used here to calculate the evaporation coefficients and the ratio of the mass of the isotopically distinct gas species (for example if the gas has significant MgO relative to Mg, or SiO_2 rather than SiO). There are several reasons why we do not subscribe to this. To begin with, when one invokes a speciation in the gas that differs from that calculated using equilibrium thermodynamics, one is in effect introducing a free parameter that needs to be determined empirically. We prefer to use the evaporation coefficient as the free parameter in that it does not imply a particular process for which there is no evidence. Indeed what experimental evidence does exist (Nichols et al., 1998) indicates that the dominant gas phase species over evaporating forsterite are indeed the thermodynamically stable ones Mg and SiO. What is needed is a better molecular level understanding of what takes place at the evaporation surface. Our hope is that experimental results such as those reported here for the magnitude and temperature dependence of the evaporation coefficients of silicon and magnesium, and for the kinetic isotope fractionation factor for magnesium, will both encourage and constrain new theoretical efforts to understand evaporation from silicate liquids at the molecular level.

ACKNOWLEDGMENTS

We thank Denton Ebel for providing us with calculated compositions along evaporation trajectories that we used to compare with our measured data. We also thank the Field Museum for their support of the Isotope Geochemistry Laboratory. We are grateful to Shogo Tachibana for an especially constructive review. This work was supported by NASA Grants NAG5-13027 to FMR, NAG5-12997 and NNG06-6F19G to AMD, and NAG5-12077 and NNG05-GG22G to MW.

APPENDIX A. EFFECT OF RECONDENSATION ON THE ISOTOPIC FRACTIONATION OF EVAPORATION RESIDUES

The prevailing view has been that recondensation reduces the kinetic isotopic fractionation of evaporating species (Tsuchiyama et al., 1999; Humayun and Cassen, 2000; Ozawa and Nagahara, 2001;Wang et al., 2001; Richter et al., 2002), and this will be the case for virtually all natural settings. A detailed derivation of the effect of recondensation on the kinetic isotope fractionation factor was given by Richter et al. (2002) for the specific case of evaporation into an unconfined surrounding gas of finite pressure. Their equation relating the realized fractionation factor $\alpha'_{1,2}$ to that which would apply for evaporation into a vacuum ($\alpha_{1,2}$) is

$$\alpha'_{1,2} - 1 = (\alpha_{1,2} - 1)\left(1 - \frac{P_i}{P_{i,\mathrm{sat}}}\right) + \left(\frac{D_{i,1}}{D_{i,2}} - 1\right)\frac{P_i}{P_{i,\mathrm{sat}}}, \tag{A.1}$$

where $\alpha'_{1,2}$ is the effective kinetic isotope fractionation factor for isotopes 1 and 2 of element i when there is a finite pressure P_i at the evaporating surface due to diffusion of the evaporating species in the surrounding gas, $\alpha_{1,2}$ is the isotope fractionation factor in the vacuum limit, and $D_{i,1}$ and $D_{i,2}$ are the diffusion coefficients of isotopes 1 and 2 in the gas surrounding the sample. The first term on the right hand side of Eq. (A.1) is usually assumed to be the more important one and it has the effect of reducing the amount of isotopic fractionation for a given amount of the parent element evaporated. The second term, which accounts for isotopic fractionation during transport away from the surface though the surrounding gas, will be small when that gas is hydrogen (see Fig. 13 in Richter et al., 2002). The reason for this is that the ratio of the diffusion coefficients of the evaporating species in hydrogen are proportional to the inverse square root of the reduced mass $\mu_i = (m_i m_{\mathrm{H}_2})/(m_i + m_{\mathrm{H}_2})$, thus $D_{i,1}/D_{i,2} = \sqrt{(m_2(m_1+2))/(m_1(m_2+2))}$, which is sufficiently close to one to make the second term on the right hand side of Eq. (A.1) negligible compared to the first term. Thus in the specific case of evaporation into to a surrounding gas of low molecular weight it is expected that the isotopic fractionation will be reduced, and it is this that has led to the concern that the laboratory measured isotopic fractionations of evaporation residues might be smaller than expected because of recondensation.

One needs to keep in mind that evaporating into a confined space such as a vacuum furnace is not the same as evaporating into an unconfined surrounding gas. Below, we derive what, at first sight, might be a somewhat surprising result that recondensation in a finite conductance furnace can actually increase the isotopic fractionation of evaporation residues. Eq. (1) (with $n_i = 1$) can be used to write the mass conservation equation for a volatile species i in an evaporation residue as

$$V_{\mathrm{c}}\frac{\mathrm{d}\rho_i}{\mathrm{d}t} = -\frac{\gamma_i P_{i,\mathrm{sat}}(1 - P_i/P_{i,\mathrm{sat}})A}{\sqrt{2\pi m_i RT}}, \tag{A.2}$$

where ρ_i is the molar density of i in a condensed phase of volume V_{c} and surface area A. The conservation equation for i in a volume V_{g} of gas surrounding the evaporating source is

$$V_{\mathrm{g}}\frac{\mathrm{d}\rho_i^{\mathrm{gas}}}{\mathrm{d}t} = \frac{\gamma_i P_{i,\mathrm{sat}}(1 - P_i/P_{i,\mathrm{sat}})A}{\sqrt{2\pi m_i RT}} - F_i, \tag{A.3}$$

where F_i is the flux (in mol s^{-1}) other than recondensation removing i from the gas. When these conservation equations are used for a furnace with finite gas conductance around the evaporating sample, there is a relationship between the pressure P_i in the volume V_g and the flux F_i that depends on the gas conductance U_i as given by

$$F_i = \frac{U_i(P_i - P_{i,\infty})}{RT} = \frac{U_i P_i}{RT}, \tag{A.4}$$

where $P_{i,\infty}$ represents the pressure of i outside the volume V_g. In our application, the volume V_g is the region around the evaporating sample enclosed by the heating elements and heat shields and which has a finite conductance for gas species going into the surrounding vacuum chamber at $P_{i,\infty} < 10^{-6}$ Torr, which for our purposes is effectively zero. The gas conductance U_i in the molecular regime (i.e., when the mean free path of i is large compared to the linear dimensions of V_g) is of the form $U_i = G\sqrt{RT/m_i}$, where G is a geometric factor that depends on shape of the enclosing volume. For example, for a cylinder of diameter d and length l the geometric factor is $\pi d^3/((4d+3l)\sqrt{2\pi})$. The value of G for the complicated geometry of materials surrounding samples in our vacuum furnace is not known, but the relevant point is that it is a constant that does not depend on the particular species involved. Eq. (A.4) can thus be written as

$$F_i = \frac{GP_i}{\sqrt{m_i RT}} \tag{A.5}$$

Using Eq. (A.5) together with the ideal gas law $\rho_i^{\text{gas}} = P_i/RT$, we can now write the conservation of gas species as

$$\frac{V_g}{RT}\frac{\mathrm{d}P_i}{\mathrm{d}t} = \frac{\gamma_i P_{i,\text{sat}}(1 - P_i/P_{i,\text{sat}})A}{\sqrt{2\pi m_i RT}} - \frac{GP_i}{\sqrt{m_i RT}}. \tag{A.6}$$

The time scale τ_{evap} over which the evaporating system as a whole evolves will be of the order of the time it takes the evaporation flux $J_i A$ (in units of mol s^{-1}) to remove $\rho_i V_c$ moles of i from the condensed phase. Thus, $\tau_{\text{evap}} = \rho_i V_c / J_i A$. The pressure P_i in the gas surrounding the evaporating sample will evolve on two distinct time scales. The first of these is a fast time scale, τ_{gas}, corresponding to how long it takes the evaporation flux to increase the pressure P_i in the surrounding gas so that the terms on the right hand side of Eq. (A.6) come into balance. Once this balance is established, the further evolution of P_i will be governed by the much slower evolution of $P_{i,\text{sat}}$, which is determined by the composition of the condensed phase evolving on time scale τ_{evap}. The effect of these two time scales can be made explicit by dividing Eq. (A.6) by $\gamma_i P_{i,\text{sat}} A/\sqrt{2\pi m_i RT}$. Eq. (A.6) becomes

$$\frac{\sqrt{2\pi m_i RT}}{\gamma_i P_{i,\text{sat}} A}\left(\frac{V_g P_{i,\text{sat}}}{RT}\right)\frac{\mathrm{d}P_i'}{\mathrm{d}t} = (1 - P_i') - \frac{G\sqrt{2\pi}P_i'}{\gamma_i A}, \tag{A.7}$$

or equivalently

$$\left\{\frac{\frac{M_{i,\text{sat}}}{J_i A}}{\frac{M_{i,\text{cond}}}{J_i A}}\right\}\frac{\mathrm{d}P_i'}{\mathrm{d}t'} = \left\{\frac{M_{i,\text{sat}}}{M_{i,\text{cond}}}\right\}\frac{\mathrm{d}P_i'}{\mathrm{d}t'} = (1 - P_i') - \frac{G\sqrt{2\pi}P_i'}{\gamma_i A}, \tag{A.8}$$

where we introduced a nondimensional time t' scaled by the evaporation time τ_{evap}, used the fact that $J_i = \gamma_i P_{i,\text{sat}}/\sqrt{2\pi m_i RT}$; we define $M_{i,\text{sat}} = V_g P_{i,\text{sat}}/RT$, where $M_{i,\text{sat}}$ is the moles of i in V_g required to saturate the gas, and $M_{i,\text{cond}} = \rho_i V_c$. $P_i' = P_i/P_{i,\text{sat}}$ is the nondimensional pressure measured as a fraction of the saturation pressure. Eq. (A.8) reflects the fact that the ratio of the fast time scale for the evolution of the pressure to the slower time scale for the evolution of the condensed phase is simply the fraction of the moles of i in the condensed phase that would be required to saturate the volume V_g. For present purposes, the important point is that the time derivative term in Eq. (A.8) will be negligibly small for our vacuum experiments because $M_{i,\text{sat}} \ll M_{i,\text{cond}}$ and thus the pressure surrounding the evaporating material is given by a balance between the two terms on the right hand side. Thus,

$$P_i' = \frac{1}{1 + \frac{G\sqrt{2\pi}}{\gamma_i A}} = \frac{1}{1 + \frac{G^*}{\gamma_i}}, \tag{A.9}$$

where for simplicity we introduce $G^* = G\sqrt{2\pi}/A$.

Starting from Eq. (6), and assuming that equilibrium fractionations are negligible so that the saturation vapor pressure of an isotopically distinct gas species is proportional to the abundance of that isotope in the condensed phase, we can write

$$\alpha_{ik} = \frac{\left(\frac{J_i}{J_k}\right)}{\left(\frac{N_i}{N_k}\right)} = \frac{\left(\frac{J_i}{J_k}\right)}{\left(\frac{P_{i,\text{sat}}}{P_{k,\text{sat}}}\right)}, \tag{A.10}$$

which, using Eq. (1) for the evaporation fluxes, becomes

$$\alpha_{ik} = \frac{\frac{\gamma_i(1-P_i')}{\sqrt{2\pi m_i RT}}}{\frac{\gamma_k(1-P_k')}{\sqrt{2\pi m_k RT}}} \tag{A.11}$$

We now use Eq. (A.9) to write an explicit relationship between the kinetic isotope fractionation factor and the gas conductance in the vicinity of the evaporating sample,

$$\alpha_{ik} = \left[\frac{\gamma_i}{\gamma_k}\sqrt{\frac{m_k}{m_i}}\right] \times \left(\frac{1 - \frac{1}{1+G^*/\gamma_i}}{1 - \frac{1}{1+G^*/\gamma_k}}\right). \tag{A.12}$$

The quantity in square brackets is the kinetic isotope fractionation factor for evaporation into vacuum (i.e., in the limit $G^* \to \infty$). Fig. A1 shows that when $\gamma_i/\gamma_k \neq 1$, the effect of decreasing gas conductance is to make the kinetic isotope fractionation tend towards the inverse square root of the mass (i.e. $\alpha_{ik} \to \sqrt{m_k/m_i}$ as $G^* \to 0$). In other words, as the gas conductance decreases and the pressure around the samples increases, there will be more recondensation but the isotopic fractionation actually *increases*. The effect of recondensation when evaporating into a confined gas is opposite to that for evaporating into an unconfined gas. We found this result sufficiently unintuitive that we decided to check it using numerical methods to solve the full governing equations given by Eqs. (A.2) and (A.6). Fig. A2 uses the numerical results to confirm and illustrate how the calculated isotopic fractionation of evaporation residues run in a vacuum furnace depends on the gas conductance for evaporating species leaving the vicinity of the sample. As G^* becomes sufficiently small, the flux increasingly reflects the isotopic fractionation associated with the removal of the gas from the vicinity of the sample, which according to Eq. (A.5) will depend on the inverse square root of the mass of the gas species, regardless of the ratio

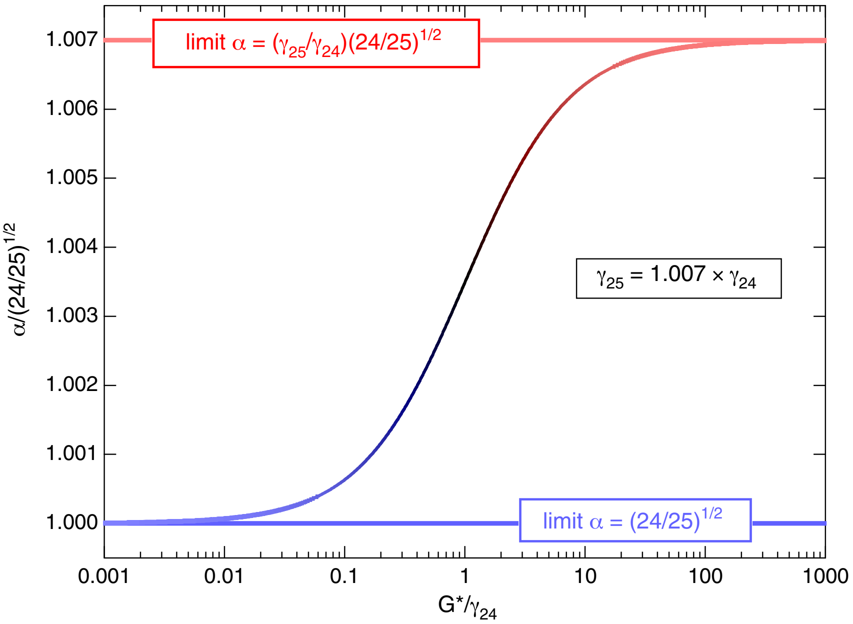

Fig. A1. Curve illustrating the effect of the finite gas conductance of a vacuum furnace on the magnesium kinetic isotopic fractionation factor of the evaporation residues. The effect of finite gas conductance for magnesium is measured by the quantity G^*/γ_{24} (see Eq. (A.12)), where G^* is proportional to the conductance and γ_{24} is the evaporation coefficient for ^{24}Mg. When the gas conductance of the furnace is sufficiently large (i.e., effective removal of the evaporated species by a negligibly small pressure difference between the sample and the far field) the isotopic fractionation factor will be that of the evaporating surface (i.e., for ^{25}Mg/^{24}Mg, $\alpha = (\gamma_{25}/\gamma_{24})\sqrt{24/25}$ with $\gamma_{25}/\gamma_{24} = 1.007$ used for purposes of illustration in this example). With decreasing conductance (smaller G^*/γ_{24}) the isotopic fractionation factor becomes increasingly affected by the fractionation associated with the removal of the gas from the vicinity of the sample, which according to the kinetic theory of gases in the molecular regime will correspond to a ratio of the fluxes equal to the inverse square root of the mass of the evaporating species (i.e.,$\alpha \rightarrow \sqrt{24/25}$).

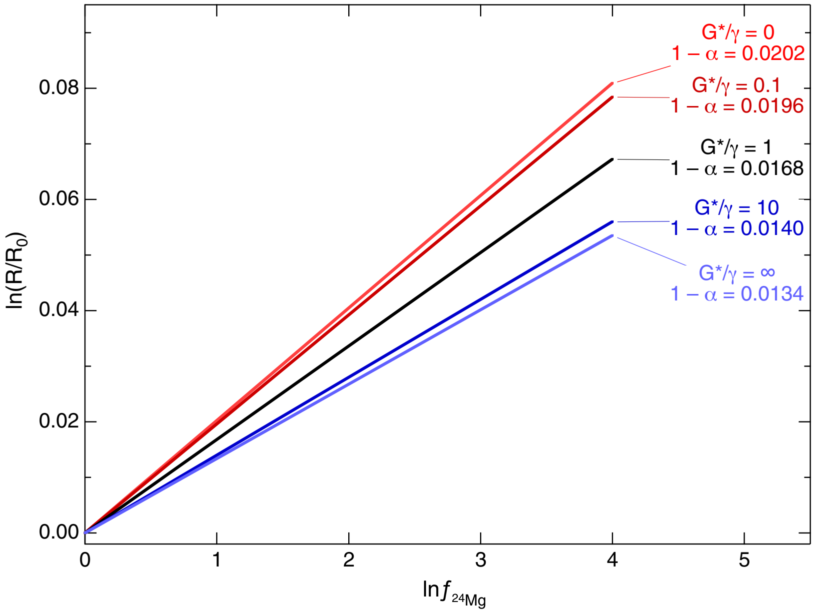

Fig. A2. Calculated isotope fractionation curves of ln(R/R_0) ($R = {}^{25}$Mg/^{24}Mg with R_0 the unfractionated ratio) as a function of $-\ln f^{24}$Mg (f^{24}Mg is the fraction of ^{24}Mg evaporated) for various choices for the gas conductance parameter G^*/γ_{24} from numerical integrations of the conservation Eqs. (A.2) and (A.8) for magnesium evaporating in a furnace of finite gas conductance. The slope of lines in such a plot corresponds to the value of $1 - \alpha$ used as the exponent in the Rayleigh fractionation Eq. (7). The calculation assumes that 1% of the magnesium in the condensed phase is sufficient to saturate the surrounding volume if there were no removal of the gas from the system, and as in Fig. A1, we assumed for purposes of illustration that the evaporation from the surface is characterized by $\gamma_{25}/\gamma_{24} = 1.007$. The results are the same as shown in Fig. A1, with the isotopic fractionation for a given amount of magnesium evaporated increasing as the gas conductance of the furnace (i.e., G^*/γ_{24}) decreases. In the limit of low gas conductance ($G^*/\gamma_{24} \rightarrow 0$), $1 - \alpha \rightarrow 1 - \sqrt{24/25}$.

γ_i/γ_k. The key point is that recondensation due to finite gas conductance will, if anything, *increase* kinetic isotopic fractionations and thus it cannot be the reason the magnesium isotopic composition of laboratory evaporation residues are consistently less than what one calculates on the assumption that $\alpha_{ik}^{\mathrm{Kin}} = \sqrt{m_k/m_i}$. While we do not know the actual value of G^* for experiments run in our vacuum furnace, we do know that G^* is inversely proportional to the surface area of the evaporating sample. This is what allowed us to use the measured isotopic composition of evaporation residues of different surface areas (i.e., different G^*) to determine whether our results have been affected by recondensation and whether the fractionation factors we report correspond to the actual values of α_{ik}.

REFERENCES

Amelin Y. (2006) The prospect of high-precision Pb isotopic dating of meteorites. *Meteorit. Planet. Sci.* **41**, 1445–1456.

Amelin Y., Krot A. N., Hutcheon I. D. and Ulyanov A. A. (2002) Lead isotopic ages of chondrules and calcium-aluminum-rich inclusions. *Science* **297**, 1678–1683.

Berman R. G. (1983). A thermodynamic model for multicomponent melts, with application to the system CaO–MgO–Al_2O_3–SiO_2. Ph.D. thesis, Univ. British Columbia.

Clayton R. N., Hinton R. W. and Davis A. M. (1988) Isotopic variations in the rock-forming elements in meteorites. *Phil. Trans. R. Soc. Lond.* **A325**, 483–501.

Dauphas N., Janney P. E., Mendybaev R. A., Wadhwa M., Richter F. M., Davis A. M., van Zuilen A., Hines R. and Foley C. N. (2004) Chromatographic separation and multicollection-ICPMS anaysis of iron. Invstigating mass-dependent and -independent isotope effects. *Anal. Chem.* **76**, 5855–5863.

Davis A. M., Hashimoto A., Clayton R. N. and Mayeda T. K. (1990) Isotope mass fractionation during evaporation of forsterite (Mg_2SiO_4). *Nature* **347**, 655–658.

Ebel D. S. (2006) Condensation of rocky material in astrophysical environments. In *Meteorites and the Early Solar System II* (eds. D. S. Lauretta and H. Y. McSween Jr.). University of Arizona Press, Tucson, pp. 253–277.

Galy A., Belshaw N. S., Halicz L. and O'Nions R. K. (2001) High-precision measurement of magnesium isotopes by multiple-collector inductively coupled plasma mass spectrometry. *Int. J. Mass Spectrom.* **208**, 89–98.

Galy A., Yoffe O., Janney P. E., Williams R. W., Cloquet C., Alard O., Halicz L., Wadhwa M., Hutcheon I. D., Ramon E. and Carignan J. (2003) Magnesium isotope heterogeneity of the isotopic standard SRM980 and new reference materials fo magnesium-isotope-ratio measurements. *J. Anal. At. Spectrom.* **18**, 1352–1356.

Ghiorso M. S. and Sack R. O. (1995) Chemical mass transfer in magmatic processes. IV. A revised and internally consistent thermodynamic model for the interpolation and extrapolation of liquid–solid equilibria in magmatic systems at elevated temperatures and pressures. *Contrib. Mineral. Petrol.* **119**, 197–212.

Grossman L. (1972) Condensation in the primitive solar nebula. *Geochim. Cosmochim. Acta* **36**, 597–619.

Grossman L. (1980) Refractory inclusions in the Allende meteorite. *Annu. Rev. Earth Planet. Sci.* **8**, 559–608.

Grossman L., Ebel D. S., Simon S. B., Davis A. M., Richter F. M. and Parsad N. M. (2000) Major element chemical and isotopic compositions of refractory inclusions in C3 chondrites: the separate roles of condensation and evaporation. *Geochim. Cosmochim. Acta* **64**, 2879–2894.

Grossman L., Ebel D. S. and Simon S. B. (2002) Formation of refractory inclusions by evaporation of condensate precursors. *Geochim. Cosmochim. Acta* **66**, 145–161.

Grossman L. and Fedkin A. V. (2003) CaO–MgO–Al_2O_3–SiO_2 liquids: Chemical and isotopic effects of Mg and Si evaporation in a closed system of solar composition. *Geochim. Cosmochim. Acta* **67**, 4205–4221.

Hashimoto A. (1990) Evaporation kinetics of forsterite and implications for the early solar nebula. *Nature* **347**, 53–55.

Hirth J. P. and Pound G. M. (1963) *Condensation and Evaporation Nucleation and Growth Kinetics*. Macmillan, New York, 191 p.

Janney P. E., Richter F. M., Davis A. M., Mendybaev R. A. and Wadhwa M. (2005) In *Lunar Planet. Sci. XXXVI*. The Lunar Planetary Institute, Houston (CD-ROM). #2123 (abstr.).

Lange R. A. and Carmichael I. S. E. (1987) Densities of Na_2O–K_2O–CaO–MgO–FeO–Fe_2O_3–Al_2O_3–TiO_2–SiO_2 liquids: new measurements and derived partial molar properties. *Geochim. Cosmochim. Acta* **51**, 2931–2946.

Larimer J. W. and Anders E. (1967) Chemical fractionations in meteorites. II. Abundance patterns and their interpretation. *Geochim. Cosmochim. Acta* **31**, 1239–1270.

MacPherson G. J., Paque J. M., Stolper E. and Grossman L. (1984) The origin and significance of reverse zoning in melilite from Allende Type B inclusions. *J. Geol.* **92**, 289–305.

Mendybaev R. A., Davis A. M. and Richter F. M. (2003) Evaporation of CMAS-liquids under reducing conditions: constraints on the formation of the melilite mantle of Type B1 CAIs. *Meteorit. Planet. Sci.* **38**, A100.

Mendybaev R. A., Richter F. M. and Davis A. M. (2006) Crystallization of melilite from CMAS-liquids and the formation of the melilite mantle of Type B1 CAIs: experimental simulations. *Geochim. Cosmochim. Acta* **70**, 2622–2642.

Nichols, Jr., R. H., Grimley R. T. and Wasserburg G. J. (1998) Measurement of gas-phase species during Langmuir evaporation of forsterite. *Meteorit. Planet. Sci.* **33**, A115.

Ozawa K. and Nagahara H. (2001) Chemical and isotopic fractionation by evaportion and their cosmochemical implications. *Geochim. Cosmochim. Acta* **65**, 2171–2199.

Petaev M. I. and Wood J. A. (2005) Meteoritic constraints on temperatures, pressures, cooling rates, chemical composition, and modes of condensation in the solar nebula. In *Chondrites and the Protoplanetary Disk*, vol. 341 (eds. A. N. Krot, E. R. D. Scott, B. Reipurth), pp. 373–406. *ASP Conference Series*.

Richter F. M. (2004) Timescales determining the degree of kinetic isotope fractionation by evaporation and condensation. *Geochim. Cosmochim. Acta* **68**, 4971–4992.

Richter F. M., Davis A. M., Ebel D. S. and Hashimoto A. (2002) Elemental and isotopic fractionation of Type B calcium-, aluminum-rich inclusions: experiments, theoretical considerations, and constraints on their thermal evolution. *Geochim. Cosmochim. Acta* **66**, 521–540.

Richter F. M., Janney P. E., Mendybaev R. A., Davis A. M. and Wadhwa M. (2005) On the temperature dependence of the kinetic isotope fractionation of Type B CAI-like melts during evaporation. In *Lunar Planet Sci. XXXVI*. The Lunar and Planetary Institute, Houston (CD-ROM). #2124.

Richter F. M., Mendybaev R. A. and Davis A. M. (2006) Conditions in the protoplanetary disk as seen by the Type B CAIs. *Meteorit. Planet. Sci.* **41**, 83–93.

Simon S. B., Grossman L., Hutcheon I. D., Williams R. W., Galy A., Fedkin A. V., Clayton R. N. and Mayeda T. K. (2004) In *Lunar Planet. Sci. XXXV*. The Lunar and Planetary Institute, Houston (CD-ROM). #1684 (abstr.).

Stolper E. (1982) Crystallization sequences of Ca-Al-rich inclusions from Allende: an experimental study. *Geochim. Cosmochim. Acta* **46**, 2159–2180.

Stolper E. and Paque J. M. (1986) Crystallization sequences of Ca-Al-rich inclusions from Allende: the effects of cooling rate and maximum temperature. *Geochim. Cosmochim. Acta* **50**, 1785–1806.

Tsuchiyama A., Takahashi T. and Tachibana S. (1999) Evaporation rates of forsterite in the primordial solar nebula: rates and accompanied isotopic fractionation. *Geochim. Cosmochim. Acta* **63**, 2451–2466.

Urey H. C. (1952) Condensation processes and the origin of the major and terrestrial planets. In *L. Farkas Memorial Volume* (ed. A. Farkas and E. P. Wigner), Research Council of Israel, Publ. No. 1, Jerusalem, p. 3.

Wang J., Davis A. M., Clayton R. N. and Mayeda T. K. (1994) Kinetic isotope fractionation during the evaporation of the iron oxide from liquid state. In *Lunar Planet. Sci*, Vol. 25, pp. 1459–1460. Lunar Planet. Sci. The Lunar and Planetary Institute, Houston.

Wang J., Davis A. M., Clayton R. N. and Hashimoto A. (1999) Evaporation of single crystal forsterite: Evaporation kinetics, magnesium isotope fractionation, and implications of mass-dependent isotopic fractionation of a diffusion-controlled reservoir. *Geochim. Cosmochim. Acta* **63**, 953–966.

Wang J., Davis A. M., Clayton R. N., Mayeda T. K. and Hashimoto A. (2001) Chemical and isotopic fractionation during the evaporation of the FeO–MgO–SiO_2–CaO–Al_2O_3–TiO_2-REE melt system. *Geochim. Cosmochim. Acta* **65**, 479–494.

Williamson J. H. (1968) Least-squares fitting of a straight line. *Can. J. Phys.* **46**, 1845–1847.

Yamada M., Tachibana S., Nagahara H. and Ozawa K. (2006) Anisotropy of Mg isotopic fractionation during evaporation and Mg self-diffusion of forsterite in vacuum. *Planet. Space Sci.* **54**, 1096–1106.

Yu Y., Hewins R. H., Alexander C. M. O'D. and Wang J. (2003) Experimental study of evaporation and isotopic mass fractionation of potassium in silicate melts. *Geochim. Cosmochim. Acta* **67**, 773–786.

Associate editor: Hiroko Nagahara